Ore Geology Reviews 91 (2017) 296–315

Contents lists available at ScienceDirect

Ore Geology Reviews

journal homepage: www.elsevier.com/locate/oregeorev

# Cu-rich porphyry magmas produced by fractional crystallization of oxidized fertile basaltic magmas (Sangnan, East Junggar, PR China)

Xing-Wang Xu[a,b,c,*], Hao Li[a,b], Stephen G. Peters[d], Ke-Zhang Qin[a,b,c], Qian Mao[a], Qi Wu[e], Tao Hong[a,b], Chu Wu[a], Guang-Lin Liang[f], Zhen-Feng Zhang[f], Lian-Hui Dong[f]

[a] Key Laboratory of Mineral Resources, Institute of Geology and Geophysics, Chinese Academy of Sciences, Beijing 100029, PR China
[b] University of Chinese Academy of Sciences, Beijing 100049, PR China
[c] Xinjiang Research Center for Mineral Resources, Chinese Academy of Sciences, Urumqi 830011, PR China
[d] United States Geological Survey, Reno, Nevada 89557, United States
[e] The Information Center of Ministry of Land and Resources of People's Republic of China, Beijing 100812, PR China
[f] Xinjiang Bureau of Geology and Mineral Resources, Xinjiang, Urumqi 830000, PR China

ARTICLE INFO

*Keywords:*
Cu-rich mafic porphyritic enclave
Porphyry Cu deposit
High-Cu magma
Fractional crystallization
Oxidized basaltic magma

ABSTRACT

The concentration of Cu is crucial to the formation of porphyry Cu deposits. However, key petrologic evidence for the origin of Cu-rich magmas is scarce. Here, we describe newly discovered Cu-rich mafic porphyritic enclaves (CMPEs) with accumulated phenocrysts, porphyritic textures and disseminated sulfide minerals in a Carboniferous tonalite pluton in the Sangnan area, East Junggar. These CMPEs have diagnostic petrologic, geochronologic and geochemical signatures that indicate they are intruded globules of Cu-rich mafic magma. These signatures include microgranular elongated laths of zoned plagioclase, needle-shaped zircon, poikilitic K-feldspar, skeletal intergrowths of chalcopyrite and epidote, sharp contacts and different geochemical compositions than the host tonalite. They also display slight younger zircon U-Pb age but similar hornblende formation depths with their host tonalites. The host tonalites are calc-alkaline and adakitic, whereas the CMPEs are high-K calc-alkaline and dioritic and have the geochemical signature of normal arc rocks.

The CMPEs contain groundmass magnetite in the carapace and Cu-Fe sulfide minerals in the core. Most Cu-Fe sulfide minerals are interstitial. The interstitial pyrite and chalcopyrite display late magmatic-hydrothermal textures, including intergrowths of chalcopyrite with magmatic oligoclase, K-feldspar and quartz, poikilitic chalcopyrite, skeletal and myrmekite-like intergrowths of chalcopyrite and epidote and sulfide-bearing miarolitic cavities. The interstitial sulfide minerals formed closely following the crystallization of the groundmass K-feldspar and quartz, and contemporary with albite and epidote. The CMPE magmas may be related to the formation of porphyry Cu deposits. The CMPE magmas are likely to have been produced by fractional crystallization of oxidized fertile basaltic magmas in a subcrustal chamber below the host tonalite chamber. The oxidized basaltic magmas were derived from metasomatised mantle wedges. The adakitic tonalite magmas are probably formed by the partial melting of mafic lower crust, that was triggered by the intrusion of the hot basaltic magmas.

## 1. Introduction

Porphyry Cu deposits (PCDs) supply nearly three-quarters of the world's Cu (Sillitoe, 2010). They are characterized by disseminated ore minerals and vein-, stockwork- and breccia-hosted copper, molybdenum and gold minerals associated with intermediate to felsic porphyritic intrusions, mostly at convergent plate margins (Lowell and Guilbert, 1970; Titley and Beane, 1981; Seedorff et al., 2005; Cooke et al., 2005; Richards, 2011). Additionally, they typically form by the precipitation of hydrothermal minerals from aqueous solutions, and are magmatic hydrothermal deposits (Hedenquist and Lowenstern, 1994; Halter et al., 2002). The ore fluids of PCDs are magmatic (Lowenstern et al., 1991;Harris et al., 2003, 2004; Heinrich et al., 2004), and are proposed to be exsolved from associated porphyry magmas on the basis of their close spatial-temporal association with mineralization and alteration zoning (Hedenquist and Lowenstern, 1994; Halter et al., 2002; Harris et al., 2003; Nadeau, 2015). The concentration of Cu by fractional crystallization of magmas is a key condition for the formation of

* Corresponding author at: Key Laboratory of Mineral Resources, Institute of Geology and Geophysics, Chinese Academy of Sciences, P.O. Box 9825, Beijing 100029, PR China.
*E-mail address:* xuxw@mail.iggcas.ac.cn (X.-W. Xu).

http://dx.doi.org/10.1016/j.oregeorev.2017.09.020
Received 9 June 2017; Received in revised form 15 September 2017; Accepted 27 September 2017
Available online 28 September 2017
0169-1368/ 

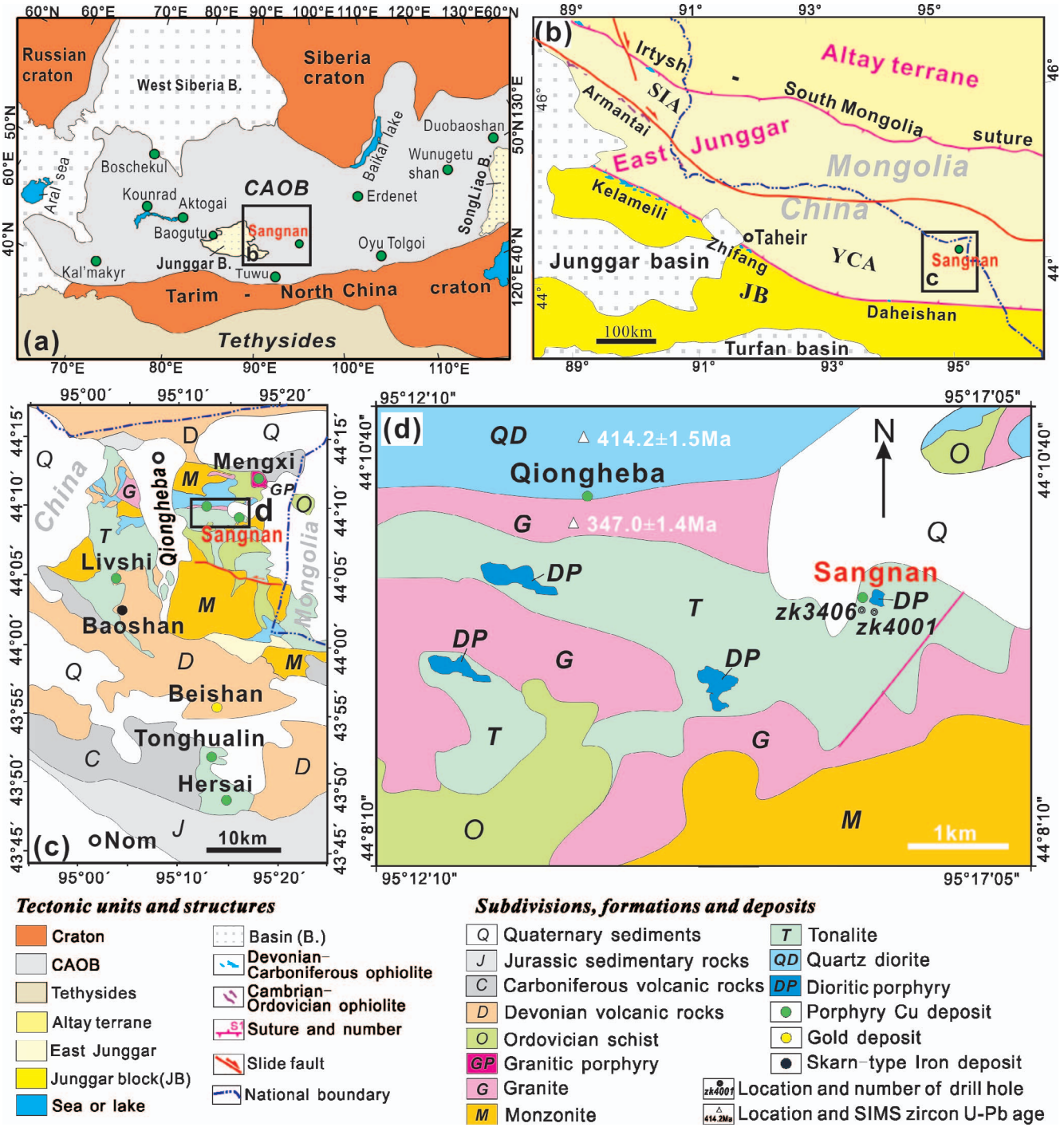


**Fig. 1.** Location (a) and tectonic units (b) of East Junggar and geological map (c) of the Qiongheba area with an enlargement of the Sangnan area (d). Figures a, b and c are after Xu et al. (2013b) and Xu et al. (2014). S1: Irtysh–South Mongolia suture, S2: Kelameili-Zhifang-Daheishan Suture. SIA: Sawuer island arc, YCA: Yemaquan continental arc.

PCDs (Candela and Holland, 1986; Hedenquist and Lowenstern, 1994; Cloos, 2001; Audétat and Pettke, 2006; Wilkinson, 2013). Therefore, the existence of Cu-rich magmas is crucial to the formation of PCDs (Core et al., 2006), which may be produced in magma chambers (Core et al., 2006; Xu et al., 2009, 2012; Sillitoe, 2010). However, the petrological evidence for the Cu-rich porphyry magmas that are produced by fractional crystallization in such magma chambers is scarce.

Recently, we discovered some Cu-rich mafic porphyritic enclaves (CMPEs) that contain accumulated phenocrysts, have porphyritic textures and also contain disseminated interstitial sulfide minerals within a tonalite pluton in the Sangnan area, East Junggar. The CMPEs provide petrologic evidence for the igneous origin of Cu-rich porphyry magmas.

## 2. Regional geological and tectonic setting

The CMPEs were observed in a tonalite pluton in the Sangnan area, in the Qiongheba porphyry Cu district in East Junggar, China (Fig. 1). The Qiongheba district lies within the eastern segment of the Paleozoic Yemaquan arc of the East Junggar terrane in the Central Asian Orogenic Belt between the Siberia and Tarim-North China cratons (Fig. 1a; Jahn et al., 2000, Jahn et al., 2004; Dong et al., 2009; Xiao et al., 2009; Xu et al., 2013b, Xu et al., 2015b). The Central Asian Orogenic Belt contains a number of world class PCDs, such as Oyu Tolgoi, Erdenet, Aktogai-Aiderly, Boschekul, Kounrad and Kal'makyr (Fig. 1a; Cooke et al., 2005; Shen et al., 2015). The East Junggar terrane, east of the Junggar

basin, is bounded by the Irtysh-South Mongolia suture in the north and by the Kelameili-Zhifang-Daheishan Devonian–Carboniferous ophiolite belt in the south (Fig. 1b). The East Junggar terrane consists from north to south of the NW-trending Sawuer Devonian oceanic island arc (SIA), the Armantai Cambrian–Ordovician ophiolite belt and the Yemaquan Paleozoic continental arc (YCA, Fig. 1b; Xu et al., 2013b). The Irtysh-South Mongolia suture that formed in the early Carboniferous represents the final closure of the Paleo-Asian Ocean between the peri-Siberia and Kazakhstan tectonic domains (e.g., Khain et al., 2003; Tong et al., 2012; Hong et al., 2015, 2017). The Yemaquan continental arc was formed by the southward subduction of the Paleo-Asian oceanic plate under the Junggar continent along the Armantai ophiolite belt in the Early Paleozoic, whereas the Sawuer oceanic island arc was related to the southward intra-oceanic subduction of the Paleo-Asian oceanic plate in the Devonian (Xu et al., 2013b). Closure of the Junggar Ocean represented by the Kelameili-Zhifang-Daheishan ophiolite belt and tectonic collision between the Yemaquan arc and Junggar block are inferred to have taken place at approximately 343 Ma in the Kelameili-Zhifang area (Zhang et al., 2013; Xu et al., 2015a).

## 3. Geological feature in the Qiongheba area

The intrusive bodies in the Qiongheba district are calc-alkaline and exhibit the geochemical signatures of continental arc rocks; rock types include quartz-diorite, tonalite, monzonite, granite, and granitic porphyry (Fig. 1c). The quartz-diorite and tonalite bodies in the Qiongheba area (Fig. 1c) are late Paleozoic and have adakite-like geochemical signatures, such as high Sr/Y ratios (> 20), high concentrations of Sr (> 400 ppm) and low concentrations of Y (< 18 ppm) and Yb (< 1.8 ppm) (Qu et al., 2009; Du et al., 2010). In the last five years, many new porphyry copper deposits and occurrences have been discovered in the Qiongheba area, such as those at Hersai, Tonghualin, Mengxi, Livshi, Sangnan and Qiongheba areas (Fig. 1c; Xu et al., 2014). The Mengxi, Tonghualin and Hersai PCDs are characterized by vein-, stockwork- and breccia-hosted mineralization (Qu et al., 2009; Du et al., 2010; Zhang et al., 2010; Xu et al., 2014), whereas the Qiongheba PCD is slightly different and is characterized more by disseminated chalcopyrite and bornite in granitic porphyry. Disseminated sulfide minerals also are prevalent in many other newly discovered PCDs in the Qiongheba district (Xu et al., 2013a). The 418 Ma albite porphyry dikes that are spatially associated with the Hersai PCD contain disseminated miarolitic, cavity-hosted chalcopyrite-sphalerite intergrowth from solid solution processes (Xu et al., 2014). The Sangnan Cu occurrence is characterized by vein-hosted mineralization associated with dioritic porphyries intruded into a tonalite stock (Fig. 2a), and by an abundance of CMPEs within the tonalite stock. These dioritic porphyries also contain some interstitial sulfide mineralization. The tonalite was emplaced into a 347 Ma granite stock adjacent to a 414 Ma quartz diorite stock (Fig. 1d).

## 4. Sample selection

The abundant CMPEs range in size from 0.5 to 20 cm and may be as large as 50 cm in diameter. They are randomly distributed in the tonalite and have variable shapes, such as rounded, ellipsoidal, discoidal, elongated, lenticular or tabular, but have sharp contacts with their host rocks (Fig. 2b and 3a and b). They are usually finer grained and darker than the tonalite host rock. They are only seen in the Sangnan area.

After petrographic examination, a total of eight CMPEs (numbered with a suffixal letter E) and eight peripheral and adjointing tonalites (numbered with a suffixal letter G), i.e. 16 samples, were selected from the drill cores in drill holes zk3406 and zk4001 for whole rock geochemistry and for Sr-Nd-Pb isotopic analysis. All the tonalite samples are unaltered. One pair (sample 6-4E and 6-4G) was selected for in situ zircon U–Pb dating and Hf isotopic analysis, 6 thin sections of the selected samples were selected for electron microprobe analysis, and 11 sulfide-bearing samples from the eight CMPEs were selected for sulfur isotopic analysis. Pairs 1-1, 1-2 and 1-3 were collected from the drill core zk4001 at depths of 118 m, 248 m and 340 m, respectively, and pairs 6-1, 6-2, 6-3, 6-4 and 6-5 were collected from the drill core zk3406 at depths of 180 m, 283 m, 420 m, 480 m and 560 m, respectively. Additionally, two dioritic porphyry samples were selected for whole rock geochemistry and Sr-Nd-Pb isotopic analysis for comparison to the CMPEs. All the analyses were conducted at the Institute of Geology and Geophysics, Chinese Academy of Sciences (IGGCAS). The analytical techniques are described in APPENDIX A. The analytical data are summarized in Tables 1 and 2 and Supplementary Tables 1–6.

## 5. Petrologic, geochemical and geochronologic features of the host tonalites

### 5.1. Petrology and mineralogy

The host tonalites with granitic texture (Fig. 3c) consist of medium-grained euhedral plagioclase (35–40 vol%), quartz (25–30 vol%), biotite (15–22 vol%), K-feldspar (5–10 vol%), hornblende (2–12 vol%), with accessory magnetite, zircon and apatite. Most plagioclases are andesine, but a few are labradorite (Supplementary Table 1, Fig. 4a). The andesine crystals are short rectangular prisms approximately 0.8- to 2.0 mm-long. The hornblendes are magnesiohornblende (Supplementary Table 2, Fig. 4b). The zircon crystals are stubby with lengths ranging from 68 to 161 μm. Some en echelon S-shaped microfractures are present in zones adjacent to the CMPEs (Fig. 3c). The host tonalites are unaltered throughout, excepting for a few replacements of hornblende by actinolite, and biotite by chlorite and/or microcrystalline anhydrite along microfractures within the andesine crystals in the narrow peripheries of the CMPEs. The Al-in-hornblende barometer of Schmidt (1992) indicates that the tonalite formed at pressures from 1.9 to 2.2 kbar (± 0.6 kbar) at depths ranging from 6.9 to 8.0 km (± 2.2 km).

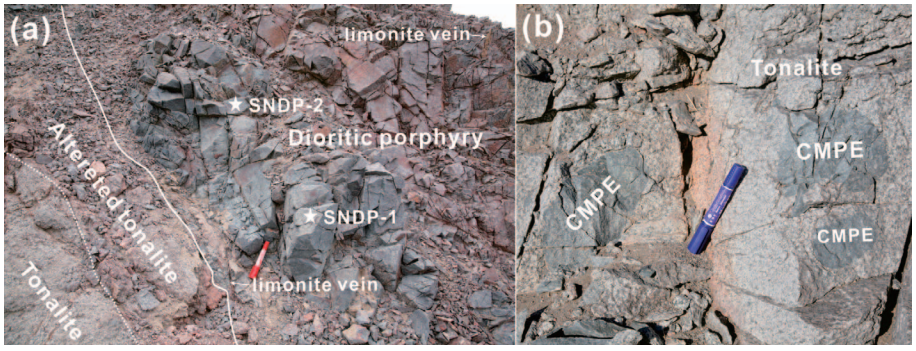


**Fig. 2.** Field photographs showing alteration and mineralization along a contact zone between a dioritic porphyry dike and tonalites (a) and distribution of CMPEs in tonalites (b) in the Sangnan area.

**Table 1**
Major (wt%) and trace element (ppm) concentration and Sm-Nd-Rb-Sr isotope composition for the CMPE, tonalite (T) and dioritic porphyry (DP) from the Sangnan area, East Junggar.

| Number | 1-1G | 1-1E | 1-2G | 1-2E | 1-3G | 1-3E | 6-1G | 6-1E | 6-2G | 6-2E | 6-3G | 6-3E | 6-4G | 6-4E | 6-5G | 6-5E | SNDP-1 | SNDP-2 |
|---|---|---|---|---|---|---|---|---|---|---|---|---|---|---|---|---|---|---|
| Rock type | T | CMPE | T | CMPE | T | CMPE | T | CMPE | T | CMPE | T | CMPE | T | CMPE | T | CMPE | DP | DP |
| Location | Drilling hole zk4001, 44°09′22.2″N, 95°15′54.4″E | | | | | | Drilling hole zk3406, 44°09′18.4″N, 95°15′49.0″E | | | | | | | | | | 44°09′26.78″N, 95°15′53.08″E | |
| | 118m | | 248m | | 340m | | 180m | | 283m | | 420m | | 480m | | 560m | | | |
| $SiO_2$ | 65.86 | 57.66 | 66.36 | 55.09 | 65.76 | 55.99 | 66.2 | 57.28 | 66.24 | 55.94 | 64.61 | 56.46 | 64.27 | 56.25 | 64.45 | 56.35 | 55.02 | 56.18 |
| $TiO_2$ | 0.4 | 0.62 | 0.39 | 0.67 | 0.37 | 0.69 | 0.38 | 0.63 | 0.4 | 0.53 | 0.45 | 0.65 | 0.38 | 0.71 | 0.43 | 0.69 | 0.68 | 0.71 |
| $Al_2O_3$ | 16.03 | 18.02 | 15.74 | 17.58 | 15.43 | 17.33 | 15.95 | 18.04 | 15.52 | 17.34 | 15.53 | 17.04 | 15.54 | 16.05 | 15.52 | 16.02 | 17.97 | 16.98 |
| $TFe_2O_3$ | 4.64 | 6.78 | 4.66 | 7.98 | 5.18 | 8.03 | 4.58 | 7.12 | 4.93 | 7.27 | 5.75 | 8.24 | 6.08 | 8.99 | 6.02 | 9.12 | 7.66 | 9.14 |
| MnO | 0.08 | 0.11 | 0.08 | 0.19 | 0.05 | 0.11 | 0.09 | 0.12 | 0.09 | 0.15 | 0.09 | 0.15 | 0.09 | 0.18 | 0.10 | 0.17 | 0.20 | 0.16 |
| MgO | 1.81 | 3.24 | 1.89 | 4.25 | 1.81 | 4.58 | 1.76 | 3.16 | 1.99 | 3.48 | 2.24 | 3.35 | 2.44 | 4.06 | 2.47 | 3.84 | 3.35 | 3.77 |
| CaO | 4.3 | 4.85 | 4.09 | 4.88 | 3.94 | 4.9 | 4.48 | 4.88 | 4.22 | 4.96 | 4.67 | 5.34 | 4.68 | 5.97 | 4.54 | 6.04 | 5.63 | 5.22 |
| $Na_2O$ | 3.86 | 4.29 | 3.83 | 4.43 | 3.71 | 4.59 | 3.88 | 4.52 | 3.71 | 4.43 | 3.77 | 4.24 | 3.51 | 3.76 | 3.51 | 3.79 | 4.27 | 4.29 |
| $K_2O$ | 1.82 | 2.36 | 1.93 | 2.65 | 2.04 | 2.49 | 1.63 | 2.24 | 1.86 | 2.38 | 1.94 | 2.46 | 2.05 | 2.12 | 2.08 | 2.1 | 2.26 | 2.48 |
| $P_2O_5$ | 0.09 | 0.14 | 0.11 | 0.13 | 0.10 | 0.15 | 0.10 | 0.14 | 0.11 | 0.14 | 0.12 | 0.15 | 0.10 | 0.12 | 0.11 | 0.11 | 0.13 | 0.10 |
| LOI | 1.04 | 1.6 | 1.14 | 2.22 | 1.76 | 1.23 | 1.10 | 1.90 | 1.12 | 2.72 | 0.98 | 1.34 | 1.08 | 2.34 | 1.18 | 2.3 | 2.48 | 0.74 |
| Total | 99.74 | 99.24 | 99.96 | 99.51 | 99.88 | 99.58 | 99.94 | 99.58 | 99.9 | 98.89 | 99.85 | 98.91 | 99.9 | 99.99 | 100.1 | 99.96 | 99.65 | 99.76 |
| FeO | 1.73 | 3.9 | 2.36 | 4.98 | 2.43 | 4.62 | 1.85 | 3.98 | 2.64 | 4.08 | 2.68 | 4.52 | 2.87 | 5.11 | 2.76 | 5.12 | 4.89 | 5.11 |
| $K_2O/Na_2O$ | 0.47 | 0.55 | 0.5 | 0.6 | 0.55 | 0.54 | 0.42 | 0.5 | 0.5 | 0.54 | 0.51 | 0.58 | 0.58 | 0.56 | 0.59 | 0.55 | 0.53 | 0.58 |
| Mg no.♣ | 0.44 | 0.49 | 0.45 | 0.51 | 0.41 | 0.53 | 0.43 | 0.47 | 0.44 | 0.49 | 0.44 | 0.45 | 0.44 | 0.47 | 0.45 | 0.45 | 0.51 | 0.45 |
| S | 130 | 2722 | 153 | 3550 | 352 | 9504 | 361 | 2912 | 226 | 4620 | 70 | 10076 | 72 | 6461 | 233 | 7192 | 1351 | 1178 |
| Sc | 8.75 | 12.96 | 7.9 | 12.01 | 9.22 | 13.1 | 7.2 | 11.78 | 7.67 | 14.95 | 7.79 | 22.68 | 6.6 | 14.81 | 6 | 13.53 | 14.27 | 28.60 |
| V | 107.3 | 175 | 88.5 | 179.5 | 78.8 | 185.6 | 98.4 | 184.6 | 97.5 | 133.3 | 119.7 | 184.7 | 95.7 | 142.9 | 100 | 138.8 | 179.74 | 156.47 |
| Cr | 6.52 | 4.63 | 29.31 | 53.5 | 22.99 | 49.55 | 96.94 | 33.62 | 10.28 | 16.52 | 4.96 | 18.13 | 51.44 | 24.19 | 6.68 | 7.11 | 37.98 | 39.80 |
| Ni | 2.77 | 5.48 | 5.12 | 10.18 | 8.38 | 7.94 | 10.81 | 5.28 | 5.65 | 9.55 | 3.77 | 10.76 | 5.08 | 8.22 | 5.23 | 9.47 | 7.50 | 10.10 |
| Co | 11.41 | 21.04 | 11.05 | 23.11 | 13.97 | 27.21 | 10.82 | 22.87 | 11.36 | 25.86 | 12.43 | 16.57 | 13.33 | 28.53 | 13.12 | 29.74 | 14.04 | 23.85 |
| Cu | 128 | 2698 | 158 | 3351 | 349 | 6408 | 119 | 2887 | 231 | 4361 | 270 | 6793 | 358 | 6404 | 355 | 7128 | 1227 | 1153 |
| Ga | 14.85 | 18.5 | 15.24 | 16.92 | 14.59 | 26.77 | 15.08 | 18.31 | 15.07 | 16.28 | 15.79 | 18.29 | 15.59 | 18.7 | 15.68 | 18.2 | 17.26 | 17.78 |
| Rb | 42.91 | 67.71 | 38.35 | 85.08 | 52.31 | 50.35 | 33.86 | 61.36 | 41.49 | 62.31 | 41.79 | 55.71 | 47.49 | 29.89 | 38.24 | 49.69 | 63.86 | 58.01 |
| Sr | 408 | 410 | 464 | 377 | 451 | 428 | 427 | 385 | 441 | 403 | 413 | 451 | 404 | 151 | 392 | 236 | 452 | 431 |
| Y | 13.38 | 27.66 | 11.13 | 24.01 | 11.57 | 24.63 | 13.28 | 29.7 | 12.32 | 22.59 | 16.28 | 30.47 | 13.18 | 20.87 | 12.18 | 20.42 | 23.09 | 26.04 |
| Zr | 98 | 115 | 99 | 47 | 100 | 39 | 100 | 73 | 97 | 54 | 133 | 48 | 95 | 45 | 111 | 38 | 70 | 84 |
| Nb | 3.89 | 4.95 | 3.31 | 4.31 | 3.77 | 6.16 | 3.52 | 5.1 | 3.63 | 4.38 | 3.88 | 5.01 | 3.3 | 4.73 | 3.9 | 4.61 | 4.79 | 4.32 |
| Cs | 2.58 | 2.77 | 2.99 | 4.21 | 2.52 | 4.38 | 1.55 | 2.51 | 2.71 | 3.33 | 2.44 | 3.49 | 2.13 | 2.93 | 1.71 | 2.92 | 4.16 | 3.23 |
| Ba | 692 | 507 | 689 | 801 | 717 | 679 | 628 | 513 | 644 | 659 | 683 | 707 | 509 | 253 | 477 | 400 | 317 | 849 |
| La | 10.25 | 14.58 | 8.44 | 8.16 | 6.65 | 7.28 | 12.63 | 9.12 | 8.49 | 8.48 | 12.73 | 14.99 | 8.23 | 12.98 | 9.26 | 23.38 | 10.82 | 17.83 |
| Ce | 20.21 | 29.48 | 16.95 | 18.89 | 18.99 | 16.19 | 24.05 | 19.89 | 17.12 | 18.27 | 25.62 | 35.22 | 16.74 | 18.99 | 19.27 | 33.24 | 23.04 | 31.09 |
| Pr | 2.59 | 3.9 | 2.2 | 2.91 | 1.62 | 2.45 | 2.99 | 2.97 | 2.3 | 2.82 | 3.47 | 5.2 | 2.26 | 3.75 | 2.51 | 5.83 | 2.97 | 5.11 |
| Nd | 9.95 | 16.11 | 9.02 | 13.51 | 6.39 | 11.32 | 11.2 | 13.7 | 9.41 | 13.02 | 13.62 | 22.9 | 8.88 | 15.63 | 9.94 | 23.59 | 12.27 | 22.81 |
| Sm | 2.4 | 3.85 | 2.01 | 3.55 | 1.54 | 3.23 | 2.32 | 3.78 | 2.31 | 3.34 | 3.11 | 5.25 | 2.06 | 3.58 | 2.37 | 4.52 | 3.74 | 5.15 |
| Eu | 0.77 | 0.88 | 0.78 | 0.91 | 0.7 | 0.91 | 0.8 | 0.88 | 0.76 | 0.83 | 0.89 | 1.3 | 0.75 | 0.79 | 0.75 | 0.85 | 0.99 | 1.02 |
| Gd | 2.33 | 4.06 | 2.06 | 3.87 | 1.79 | 3.43 | 2.31 | 4.15 | 2.27 | 3.63 | 3.1 | 5.07 | 2.16 | 3.56 | 2.23 | 4.15 | 4.32 | 5.07 |
| Tb | 0.38 | 0.75 | 0.34 | 0.69 | 0.29 | 0.67 | 0.35 | 0.82 | 0.36 | 0.66 | 0.48 | 0.86 | 0.36 | 0.63 | 0.36 | 0.65 | 0.68 | 0.84 |
| Dy | 2.32 | 4.93 | 2.06 | 4.63 | 1.93 | 4.59 | 2.21 | 5.47 | 2.17 | 4.17 | 3.03 | 5.44 | 2.26 | 3.9 | 2.22 | 3.78 | 4.36 | 5.38 |
| Ho | 0.51 | 1.09 | 0.44 | 1.01 | 0.44 | 1.07 | 0.47 | 1.23 | 0.47 | 0.91 | 0.68 | 1.18 | 0.49 | 0.84 | 0.48 | 0.78 | 0.99 | 1.15 |
| Er | 1.52 | 3.27 | 1.31 | 3.02 | 1.4 | 3.19 | 1.42 | 3.59 | 1.38 | 2.67 | 2 | 3.51 | 1.49 | 2.45 | 1.43 | 2.35 | 3.03 | 3.49 |
| Tm | 0.24 | 0.54 | 0.21 | 0.5 | 0.24 | 0.53 | 0.23 | 0.58 | 0.22 | 0.42 | 0.32 | 0.57 | 0.26 | 0.41 | 0.23 | 0.39 | 0.50 | 0.54 |
| Yb | 1.76 | 3.77 | 1.48 | 3.45 | 1.72 | 3.77 | 1.65 | 4.03 | 1.55 | 2.96 | 2.27 | 3.96 | 1.81 | 2.84 | 1.61 | 2.66 | 3.30 | 3.80 |
| Lu | 0.3 | 0.6 | 0.24 | 0.56 | 0.29 | 0.61 | 0.27 | 0.63 | 0.26 | 0.47 | 0.36 | 0.63 | 0.3 | 0.45 | 0.27 | 0.43 | 0.51 | 0.62 |
| Hf | 3.03 | 3.76 | 2.98 | 1.90 | 2.98 | 1.58 | 2.92 | 2.56 | 2.93 | 2.11 | 3.96 | 1.92 | 2.78 | 1.77 | 3.20 | 1.54 | 1.98 | 4.04 |
| Ta | 0.39 | 0.52 | 0.27 | 0.36 | 0.34 | 0.47 | 0.33 | 0.54 | 0.31 | 0.39 | 0.33 | 0.36 | 0.30 | 0.40 | 0.33 | 0.39 | 0.48 | 0.26 |
| Pb | 5.79 | 5.39 | 5.59 | 5.47 | 4.37 | 4.22 | 5.58 | 5.67 | 4.97 | 6.22 | 5.22 | 5.09 | 5.08 | 6.42 | 4.79 | 6.85 | 6.44 | 8.04 |
| Th | 2.98 | 4.31 | 2.21 | 1.67 | 2.82 | 2.80 | 2.74 | 3.82 | 2.34 | 2.33 | 3.64 | 4.31 | 3.12 | 3.41 | 2.91 | 4.43 | 1.50 | 3.18 |
| U | 1.38 | 2.48 | 1.17 | 1.28 | 1 | 1.36 | 1.05 | 3.23 | 1.1 | 1.74 | 1.19 | 2 | 1.25 | 1.64 | 1.29 | 1.57 | 1.89 | 1.05 |
| REE | 55.55 | 87.82 | 47.52 | 65.65 | 37.98 | 59.22 | 62.89 | 70.83 | 49.06 | 62.66 | 71.68 | 106.07 | 48.02 | 70.79 | 52.95 | 106.59 | 71.52 | 103.89 |
| Eu/Eu* | 1 | 0.68 | 1.17 | 0.75 | 1.28 | 0.84 | 1.06 | 0.68 | 1.02 | 0.73 | 0.88 | 0.77 | 1.09 | 0.67 | 1.0 | 0.6 | 0.75 | 0.61 |
| LaN/YbN | 3.94 | 2.61 | 3.85 | 1.6 | 2.61 | 1.3 | 5.17 | 1.53 | 3.7 | 1.94 | 3.78 | 2.55 | 3.07 | 3.08 | 3.89 | 5.92 | 2.21 | 4.3 |
| Sr/Y | 30.53 | 14.82 | 41.64 | 15.68 | 38.95 | 17.38 | 32.15 | 12.97 | 35.79 | 17.86 | 25.38 | 14.8 | 30.62 | 7.24 | 32.19 | 11.54 | 19.59 | 16.56 |
| Zr/Sm | 40.83 | 29.87 | 49.25 | 13.24 | 64.94 | 12.07 | 43.10 | 19.31 | 41.99 | 16.17 | 42.77 | 9.14 | 46.12 | 12.57 | 46.84 | 8.41 | 18.62 | 16.22 |

♣ Mg no. = Mg/(Mg+Fe), where Mg and Fe are atomic proportions.

### 5.2. Whole rock geochemistry

The host tonalites all have similar geochemical signatures (Tables 1 and 2). They have a lot of Cu (119–358 ppm). They contain 392–464 ppm Sr, 11.13–16.28 ppm Y and 1.48–2.27 ppm Yb. They are calc-alkaline (Fig. 8a).

### 5.3. Zircon U-Pb ages and Lu-Hf isotopes

Stubby zircons from tonalite 6-4G (the peripheral of the CMPE 6-4E) have $^{206}Pb/^{238}U$ ages ranging from 324.5 ± 5.4 Ma to 354.9 ± 5.2 Ma, $^{176}Hf/^{177}Hf$ values from 0.282864 to 0.282996, $\varepsilon_{Hf(t)}$ values from +10.9 to +15.4 with a weighted average of 12.72 ± 0.37 (Fig. 9b), and depleted-mantle model age ($T_{DM2(Hf)}$) from 658 Ma to 364 Ma for 30 analyzed grains (Supplementary Tables 5 and 6). Grain 10 has a much older $^{206}Pb/^{238}U$ age of 354.9 ± 5.2 Ma than others and is possibly an antecryst; the other 29 grains have a concordia age of 338.3 ± 0.95 Ma (MSWD = 0.38; Fig. 9a).

**Table 2**
Sm-Nd-Rb-Sr isotope composition for the CMPE, tonalite and dioritic porphyry from the Sangnan area, East Junggar.

| Number | 1-1G | 1-1E | 1-2G | 1-2E | 1-3G | 1-3E | 6-1G | 6-1E | 6-2G | 6-2E | 6-3G | 6-3E | 6-4G | 6-4E | 6-5G | 6-5E | SNDP-1 | SNDP-2 |
|---|---|---|---|---|---|---|---|---|---|---|---|---|---|---|---|---|---|---|
| Sm (ppm) | 1.99 | 3.37 | 1.95 | 3.34 | 1.55 | 2.45 | 2.03 | 3.54 | 1.89 | 3.22 | 2.75 | 4.48 | 2 | 3.3 | 2.06 | 4.5 | 3.61 | 3.94 |
| Nd(ppm) | 9.13 | 13.6 | 8.82 | 12.19 | 6.55 | 8.45 | 10.21 | 12.54 | 8.48 | 12.23 | 12.48 | 18.74 | 8.58 | 13.76 | 9.5 | 22.42 | 11.47 | 12.89 |
| $(^{147}Sm/^{144}Nd)_m$ | 0.132 | 0.15 | 0.12 | 0.171 | 0.131 | 0.121 | 0.141 | 0.145 | 0.135 | 0.159 | 0.134 | 0.166 | 0.133 | 0.145 | 0.143 | 0.175 | 0.137287 | 0.148916 |
| $(^{143}Nd/^{144}Nd)_m$ | 0.51277 | 0.51276 | 0.51278 | 0.51285 | 0.51278 | 0.51286 | 0.51271 | 0.51281 | 0.51278 | 0.5128 | 0.51279 | 0.51279 | 0.51275 | 0.51278 | 0.51266 | 0.51275 | 0.512777 | 0.5127863 |
| Error (2) | 0.00001 | 0.00001 | 0.00001 | 0.00001 | 0.00001 | 0.00001 | 0.00001 | 0.00001 | 0.00001 | 0.00001 | 0.00001 | 0.00001 | 0.00001 | 0.00001 | 0.00001 | 0.00001 | 0.000018 | 0.000013 |
| $(^{143}Nd/^{144}Nd)_i$ | 0.51248 | 0.51243 | 0.51244 | 0.51243 | 0.51237 | 0.51249 | 0.51244 | 0.51246 | 0.51248 | 0.51245 | 0.51248 | 0.51248 | 0.51249 | 0.51248 | 0.51246 | 0.51248 | 0.512474 | 0.512458 |
| ε(t) | 5.46 | 4.46 | 4.67 | 4.36 | 3.33 | 5.47 | 4.6 | 4.96 | 5.42 | 4.84 | 5.43 | 5.41 | 5.61 | 5.26 | 5.14 | 5.33 | 5.27 | 4.95 |
| Tdm(Ma) | 701 | 720 | 925 | 972 | 713 | 693 | 962 | 788 | 794 | 838 | 1134 | 827 | 722 | 899 | 1232 | 657 | 705 | 676 |
| Rb(ppm) | 42.76 | 67.6 | 40.27 | 94.08 | 48.43 | 60.08 | 32.66 | 62.81 | 40.7 | 70.64 | 42.68 | 69.59 | 46.65 | 65.96 | 37.13 | 71.38 | 64.6 | 63.28 |
| Sr(ppm) | 395.8 | 419 | 467.5 | 401.6 | 1704 | 477.7 | 430.5 | 395.9 | 432.5 | 419.8 | 422.5 | 465 | 405.1 | 333.7 | 375.4 | 334.5 | 498 | 446 |
| $(^{87}Rb/^{86}Sr)_m$ | 0.313 | 0.467 | 0.22 | 0.459 | 0.286 | 0.618 | 0.333 | 0.572 | 0.272 | 0.487 | 0.249 | 0.678 | 0.292 | 0.433 | 0.082 | 0.364 | 0.56100346 | 0.46011206 |
| $(^{87}Sr/^{86}Sr)_m$ | 0.70563 | 0.70623 | 0.70534 | 0.70721 | 0.7049 | 0.70583 | 0.70515 | 0.7062 | 0.70538 | 0.7064 | 0.70542 | 0.70605 | 0.70568 | 0.70681 | 0.70549 | 0.70702 | 0.7067029 | 0.706289 |
| Error (2) | 0.00001 | 0.00001 | 0.00001 | 0.00001 | 0.00001 | 0.00001 | 0.00001 | 0.00001 | 0.00001 | 0.00001 | 0.00001 | 0.00001 | 0.00001 | 0.00001 | 0.00001 | 0.00001 | 0.00001 | 0.00001 |
| $(^{87}Sr/^{86}Sr)_i$ | 0.70412 | 0.704 | 0.70409 | 0.704 | 0.70411 | 0.70406 | 0.70407 | 0.70407 | 0.70406 | 0.70407 | 0.70413 | 0.70396 | 0.70401 | 0.70398 | 0.7045 | 0.70409 | 0.70401 | 0.70405 |
| $(^{206}Pb/^{204}Pb)_m$ | 18.861 | 19.903 | 18.697 | 18.941 | 18.89 | 19.368 | 18.667 | 19.573 | 18.774 | 18.95 | 18.759 | 19.206 | 18.884 | 18.952 | 18.93 | 18.921 | 18.353 | 18.12 |
| Error (2) | 0.009 | 0.010 | 0.010 | 0.009 | 0.013 | 0.010 | 0.009 | 0.019 | 0.008 | 0.012 | 0.010 | 0.011 | 0.020 | 0.009 | 0.008 | 0.008 | 0.011 | 0.021 |
| $(^{207}Pb/^{204}Pb)_m$ | 15.521 | 15.572 | 15.524 | 15.538 | 15.511 | 15.551 | 15.531 | 15.565 | 15.538 | 15.524 | 15.51 | 15.563 | 15.528 | 15.54 | 15.515 | 15.524 | 15.473 | 15.468 |
| Error (2) | 0.010 | 0.010 | 0.010 | 0.010 | 0.015 | 0.009 | 0.010 | 0.025 | 0.008 | 0.010 | 0.010 | 0.012 | 0.023 | 0.010 | 0.009 | 0.007 | 0.011 | 0.023 |
| $(^{208}Pb/^{204}Pb)_m$ | 38.449 | 38.613 | 38.378 | 38.274 | 38.519 | 38.679 | 38.403 | 38.624 | 38.471 | 38.372 | 38.479 | 38.654 | 38.462 | 38.529 | 38.498 | 38.603 | 37.803 | 37.843 |
| Error (2) | 0.012 | 0.011 | 0.011 | 0.01 | 0.018 | 0.009 | 0.011 | 0.03 | 0.008 | 0.012 | 0.011 | 0.013 | 0.024 | 0.008 | 0.009 | 0.009 | 0.011 | 0.026 |
| $(^{206}Pb/^{204}Pb)_i$ | 18.314 | 18.046 | 17.617 | 18.026 | 18.143 | 18.01 | 18.085 | 18.042 | 18.004 | 18.015 | 18.152 | 17.982 | 17.864 | 17.983 | 18.267 | 18.103 | 17.716 | 17.884 |
| $(^{207}Pb/^{204}Pb)_i$ | 15.488 | 15.478 | 15.462 | 15.497 | 15.482 | 15.467 | 15.494 | 15.484 | 15.475 | 15.498 | 15.497 | 15.486 | 15.492 | 15.469 | 15.493 | 15.469 | 15.439 | 15.455 |
| $(^{208}Pb/^{204}Pb)_i$ | 37.715 | 37.876 | 37.871 | 37.859 | 37.885 | 37.819 | 37.941 | 37.777 | 37.957 | 37.945 | 37.937 | 37.939 | 37.71 | 37.701 | 37.938 | 37.799 | 37.465 | 37.787 |

The ages of the CMPE, tonalite and dioritic porphyry were referred as 336.7 Ma, 338.3 Ma and 336.7 Ma, respectively.

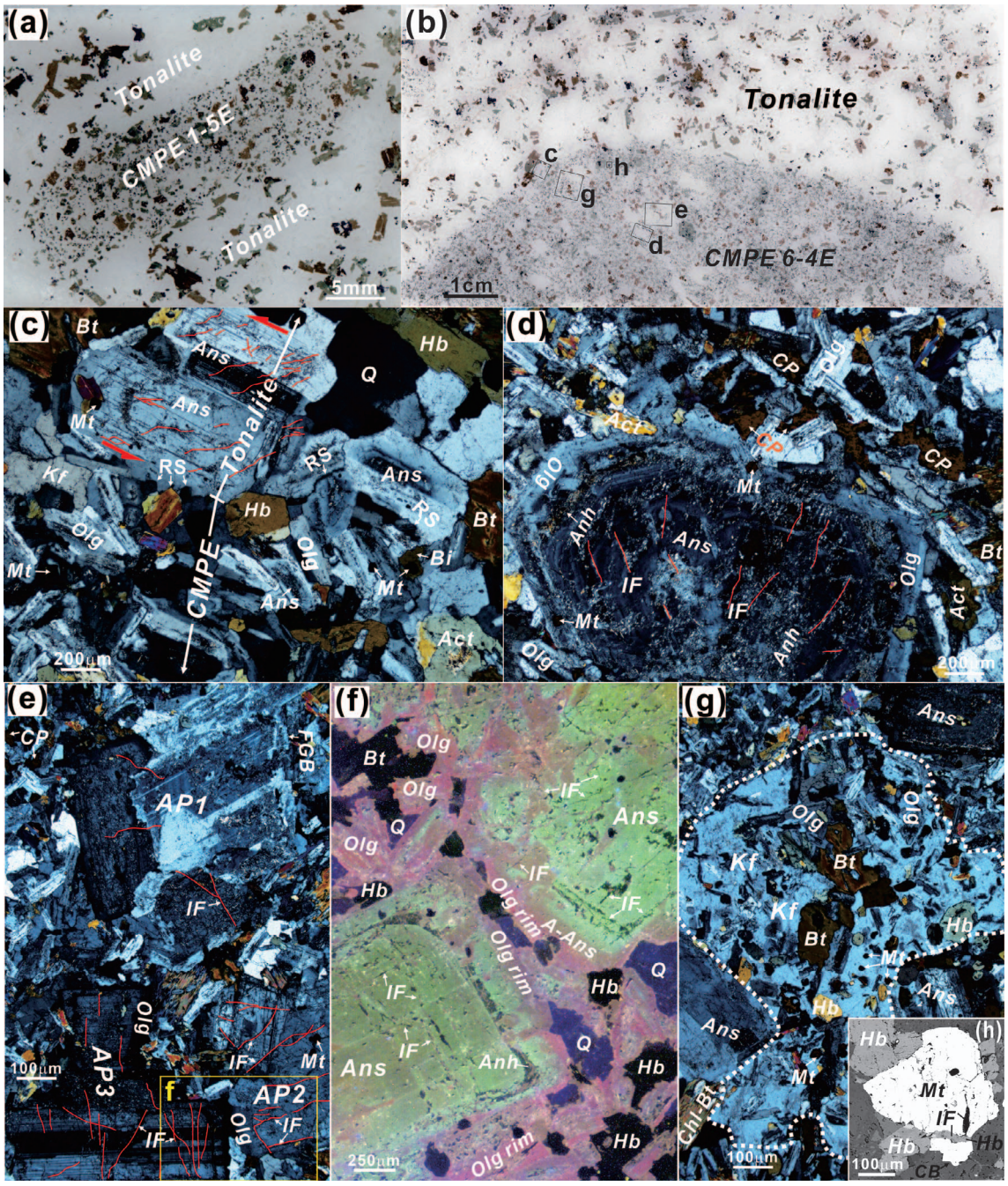


**Fig. 3.** Two scanning images (an and b) with four enlarged polarized microscopic images (c-e, g), a CL image (f) and a back scattered electron image (h) showing the shape, boundary, texture and structure of the CMPEs 1-5E and 6-4E that were collected at 260 m-depth from the drill core zk4001 and 480 m-depth from the drill core zk3406, respectively, in the Sangnan area. The episcopic illumination was superimposed for images c-e. Panels a and b show shape of two CMPEs and their relation with host tonalites in thinner section. Panel c displays contact boundary between CMPE 6-4E (lower part) and its host tonalite (upper part). Panels d, e, f, g and h show some representive textures and structrues of CMPEs. A- Ans: altered andesine, Act: actinolite, Anh: anhydrite, Ans: andesine, AP: accumulated phenocryst, Bi: biotite, Chi-Bi: chlorite transformed from biotite, CP: chalcopyrite, FGB: fractured grain boundary, GD: tonalite, Hb: hornblende, IF: intragranular or intra-glomerophyric fracture, Kf: K-feldspar, Mt: magnetite, Olg: oligoclase, RS: resorption surface. Black rectangles in panel b represent locations of panels c, d, e, g and h, whereas yellow rectangle in panel e for location of panel f. The red lines in panels c, d and e outline the represent microfractures in both the phenocrysts and ambient rocks, and the red arrow in panel c shows the shear direction. The white dot lines in panel g shows boundary of a poikilitic K-feldspar with inclusions of oligoclase, hornblende, biotite and magnetite crystals.

## 6. Petrologic, geochemical and geochronologic features of the CMPEs

### 6.1. Petrology and mineralogy

The CMPEs are characterized by porphyritic texture and by disseminated sulfide minerals (Fig. 3d and e). They contain mainly medium-grained andesine (20–30 vol%), biotite (3–10 vol%) and hornblende (2–5 vol%) phenocrysts in a fine-grained groundmass of euhedral zoned oligoclase (30–40 vol%), hornblende (5–20 vol%), biotite (5–10 vol%), K-feldspar, quartz, albite, magnetite (0.5–2 vol%), pyrite, chalcopyrite (1–5 vol%), bornite, and minor zircon, calcite, epidote and titanite. Compositional variation of earlier-formed andesine to later formed oligoclase, albite and K–feldspar is continuous (Supplementary Table 1, Fig. 4a).

The mineral content varies among the CMPEs. The andesine and

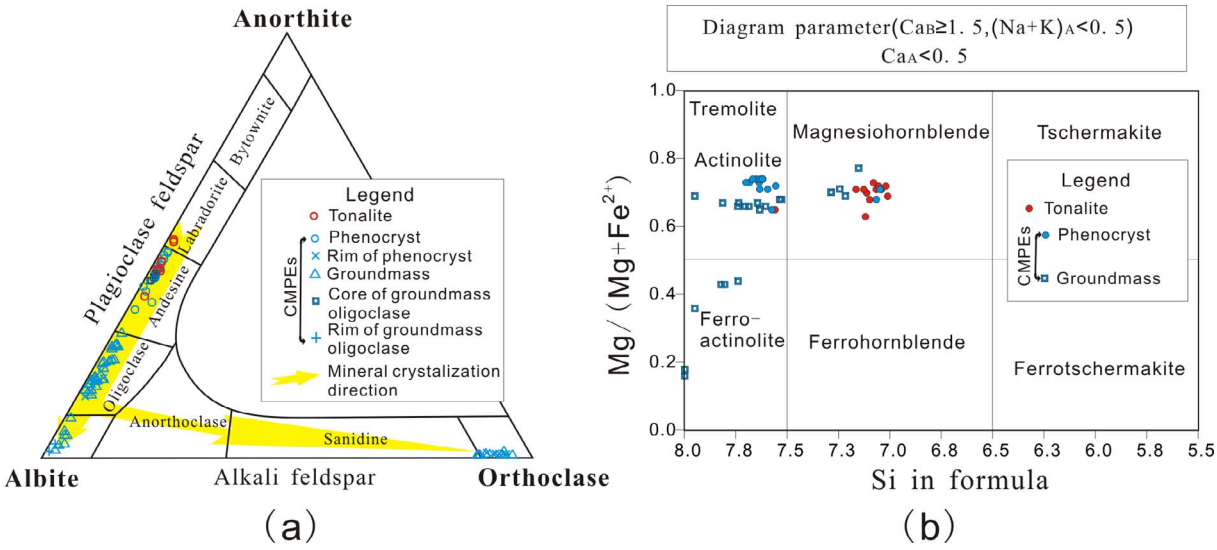


**Fig. 4.** Composition of the feldspar plotted on the Anorthite-Albite-Orthoclase diagram (a) and hornblende plotted in the nomenclature diagram after Leake et al. (1997) (b) for the CMPEs and their host tonalites in the Sangnan area.

oligoclase have distinct green and red luminescence, respectively, whereas the apatite, K-feldspar, quartz and albite have bright yellow, blue, violet and sienna luminescence, respectively (Figs. 3f, 5a and c). Most andesine phenocrysts have intensive intragranular microfractures (Fig. 3e and f), along which andesine is altered and replaced by anhydrite and magnetite. Some andesine phenocrysts are glomerophyric and form phenocryst accumulations with intensive intra-glomerophyric microfractures and with fractured grain boundaries (Fig. 3e). Both the fractured and altered andesine phenocrysts are enclosed by oligoclase or by K-feldspar rims that contain magnetite inclusions (Fig. 3d and f).

Groundmass oligoclase in the CMPEs consists of elongate rectangular prisms that are approximately 145- to 420- μm long. Some groundmass oligoclase crystals contain andesine cores with irregular leached voids, into which anhydrite and chalcopyrite were deposited (Fig. 5); however, these andesine cores contain additional leached voids and alteration anhydrite, which commonly is more voids than in their oligoclase rims (Fig. 5a and c). There are two types of K-feldspar in the CMPEs, including 1) magmatic poikilitic K-feldspar grains which contain enclosures of oligoclase, hornblende, biotite and magnetite (Fig. 3 g); and 2) groundmass K-feldspar that is intergrown with oligoclase, quartz and interstitial pyrite and chalcopyrite (Fig. 5a and c). Most quartz in the CMPEs is present as interstitial fillings within the groundmass oligoclase/K-feldspar (Fig. 3f), and also as additional intergrowths with oligoclase, K-feldspar and chalcopyrite (Fig. 5b). The sienna-colored, luminescing albite is present overprinting the groundmass oligoclase with interstitial chalcopyrite (Fig. 5a and c).

Both phenocryst and groundmass hornblendes in the CMPEs are magnesiohornblende, and some are altered to actinolite and ferro-actinolite (Supplementary Table 2, Fig. 4b). Zircon is present as two distinct species: a stubby variety with average elongation ratios of approximately 1.43, and a needle-shaped variety with elongation ratios > 2.0 and up to 5.2. Some stubby zircon crystals contain corroded boundaries with intragranular fractures enclosed by overgrowth rims.

Epidote in the CMPEs occurs in three patterns: 1) epidote included within coarse-grained interstitial chalcopyrite (Fig. 6a), but some epidote contains inclusions of chalcopyrite as dots and also displays myrmekite-like chalcopyrite-epidote intergrowth textures (Fig. 6b and c). In addition, there are a few skeletal chalcopyrite-epidote intergrowths (Fig. 6d); 2) interstitial epidote is also present in-between groundmass biotite minerals (Fig. 6e); and 3) in miarolitic intergrowths with chalcopyrite (Fig. 7b and c). The epidote minerals show overall chemical variation from 24.95 to 27.53 mol% pistacite (Ps) (Supplementary Table 3).

The CMPEs always have narrow margins that are mainly composed of elongated laths of oligoclase, hornblende, biotite and magnetite. In some contact zones, some groundmass oligoclase laths are overgrown onto partial resorption surfaces of euhedral medium-grained andesine from the ambient tonalite (Fig. 3c). Some CMPE phenocryst andesine, biotite and hornblende are altered and replaced by anhydrite, chlorite and actinolite or ferro-actinolite, respectively. Spongy andesine phenocrysts are enclosed by oligoclase rims with magnetite inclusions (Fig. 3d). Most K-feldspar is unaltered and has blue luminescence, whereas a few K-feldspar crystals adjacent to chalcopyrite replacements are altered and have dark-olive-green luminescence (Fig. 7e and f). Biotite and hornblende within the CMPE margins (Fig. 3d) and the poikilitic K-feldspar (Fig. 3g) are unaltered. The Al-in-hornblende barometer of Schmidt (1992) suggests that the groundmass hornblendes formed at pressures ranging from 1.8 to 2.1 kbar ( ± 0.6 kbar) and depths ranging from 6.5 to 7.7 km ( ± 2.2 km) (Supplementary Table 2).

Most magnetite in the CMPEs is euhedral and fine grained (30–80-μm) and is located within the CMPE margin (Fig. 3c), oligoclase rims (Fig. 3d) and poikilitic K-feldspar (Fig. 3g). A few random, coarser, angular magnetite crystals (> 200 μm and up to 450 μm) contain corroded boundaries and intragranular fractures, some of which are filled by hornblende (Fig. 3 g).

Sulfide minerals are restricted within the sulfide cores of the CMPEs that are surrounded by weakly altered or unaltered, fine-grained magnetite-oligoclase margins or carapaces. > 90 vol% of the pyrite and chalcopyrite is interstitial and lies among elongated laths of oligoclase, K-feldspar and albite (Figs. 3d, 5a and c). About 5 vol% of chalcopyrite and all bornite grains are present within miarolitic cavities that contain sulfide-epidote vugs and voids (Fig. 7a–c). Moreover, less than 5 vol% chalcopyrite is present as dot-like inclusions within epidote and calcite grains (Fig. 6d), or is also present along cleavages of actinolite and ferro-actinolite (Fig. 7d) or is associated with hydrothermal chlorite (Fig. 7e).

Fine-grained interstitial pyrite and chalcopyrite grains always are intergrown with K-feldspar and quartz (Fig. 5b). Some coarse interstitial chalcopyrite grains also have poikilitic texture and contain inclusions of hornblende, oligoclase, albite and epidote (Fig. 5d and a). Spaces for the interstitial anhedral chalcopyrite mostly are angular and irregular (Fig. 5b, 5d and 6a). The miarolitic chalcopyrite and bornite grains are spatially associated with apatite and albite (Fig. 7a and b) and are intergrown with blade-like epidote and voids (Fig. 7c). Volume of the Cu-Fe sulfide minerals is much larger than that of the volume of

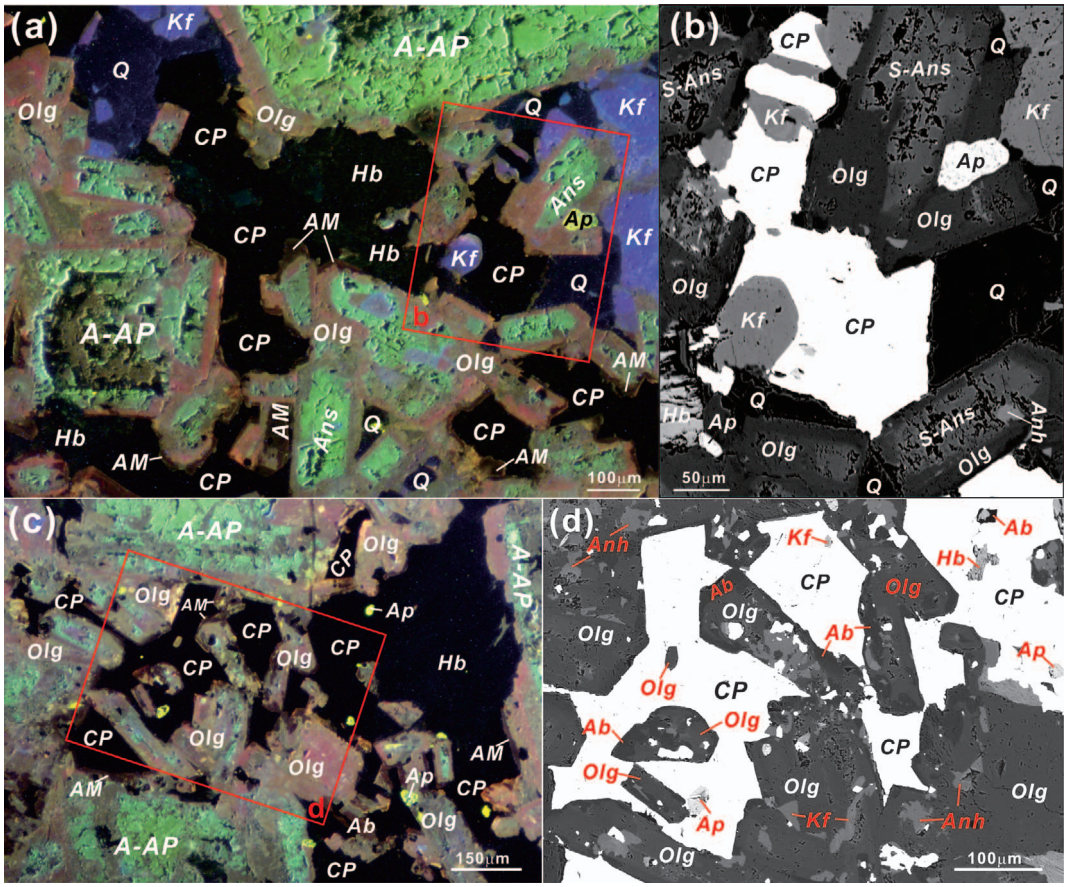


**Fig. 5.** Two CL images (a and c) with two back scattered electron images (b and d) showing the feature and distribution of interstitial apatite, K-feldspar, quartz and chalcopyrite from the CMPEs from the Sangnan area. Panel a is from the thin section 6-3E, whereas panel c from the thin section 6-2E. Red rectangles in panels a and c represent locations of panels b and d, respectively. A-AP: altered andesine phenocryst, Ab: albite, AM: albite membrane, Anh: anhydrite, Ans: andesine, Ap: apatite, Bi: biotite, CP: chalcopyrite, Hb: hornblende, Kf: K-feldspar, Olg: oligoclase, Q: quartz, S-Ans: spongy andesine.

the voids in the CPMEs. The CMPE sulfide minerals (chalcopyrite and pyrite) have sulfur compositions with $\delta^{34}S$ close to 0‰, in a limited range from +0.455 to +2.422 (Supplementary Table 4).

Crystallization of groundmass minerals within the CMPEs is continuous and orderly from andesine, hornblende, magnetite, biotite, oligoclase to interstitial apatite, K-feldspar and quartz, to albite membrane, and this includes discrete or interstitial pyrite, chalcopyrite and epidote. Precipitation of the minerals in the miarolitic cavities is also continuous starting with apatite, albite, and trending paragenetically to epidote-chalcopyrite-bornite and hydrothermal calcite and chlorite. Anhydrite, actinolite and ferro-actinolite alteration was associated with the precipitations of some chalcopyrite minerals.

### 6.2. Whole rock geochemistry

The CMPEs have similar geochemical signatures (Tables 1 and 2). They have high Cu concentrations (2698–7128 ppm). They are dioritic, and high-K calc-alkaline (Fig. 8a).

### 6.3. Zircon U-Pb ages and Lu-Hf isotopes

Needle-shaped zircons from the CMPE 6-4E have $^{206}Pb/^{238}U$ ages ranging from 320.8 ± 4.7 Ma to 347.1 ± 5.4 Ma with a concordia age of 336.7 ± 2.2 Ma (MSWD = 1.2; Fig. 9c), $^{176}Hf/^{177}Hf$ values from 0.282898 to 0.282999, $\varepsilon_{Hf\ (t)}$ values from +11.8 to +15.1 with a weighted average of 13.80 ± 0.41 (Fig. 9d), and $T_{DM2(Hf)}$ from 503 Ma to 365 Ma for 26 analyzed grains. The stubby zircons from the same CMPE 6-4E have $^{206}Pb/^{238}U$ ages ranging from 328.8 ± 5.4 Ma to 346.8 ± 5.1 Ma with a concordia age of 335.9 ± 3.0 Ma (MSWD = 0.99; Fig. 9e), $^{176}Hf/^{177}Hf$ values from 0.282889 to 0.282996, $\varepsilon_{Hf\ (t)}$ values from +11.5 to +15.2 with a weighted average of 12.89 ± 0.73 (Fig. 9f), and $T_{DM2(Hf)}$ from 608 Ma to 367 Ma for 11 analyzed grains (Supplementary Tables 5 and 6).

## 7. Discussion: Origin of the CMPEs and their host tonalites

### 7.1. Nature of the CMPEs and their host tonalites

The host tonalites in the Sangnan area, East Junggar have similar geochemical signatures to adakites (Fig. 8b), including 64.27–66.36 wt % $SiO_2$ (> 56 wt%), 1.76–2.47 wt% MgO (< 3 wt%), 3.51–3.88 wt% $Na_2O$ (> 3.5 wt%), 392–464 ppm Sr (mostly > 400 ppm), 11.13–16.28 ppm Y (< 18 ppm), 1.48–2.27 ppm Yb (mostly less than 1.8 ppm), an Sr/Y ratio of 25.38 to 41.64 (> 20), $K_2O/Na_2O$ of 0.42–0.59 (equal or close to 0.42) and $(^{87}Sr/^{86}Sr)_i$ of 0.70401–0.7045 (≤0.7045) (Defant and Drummond, 1990, 1993; Martin, 1999; Martin et al., 2005).

However, compared with type-adakites that are slab-derived melts in the western Aleutians Islands, in southernmost Chile and in Batan island in the northern Philippines (Kay, 1978; Kay et al., 1993; Schiano et al., 1995; Yogodzinski et al., 1995), the Sangnan tonalites have lower $(La/Yb)_N$ (< 10) and Ni (< 20 ppm), and lower $(^{143}Nd/^{144}Nd)_i$ and higher $(^{87}Sr/^{86}Sr)_i$. They also plot outside the field of the Middle Ocean Ridge Basalt (MORB) and of adakite in the $\varepsilon_{Nd\ (t)}$ versus $(^{87}Sr/^{86}Sr)_i$ diagram (Fig. 10a), implying that the Sangnan tonalites were not derived from slab melts. This conclusion was consistent with known evidence that the tonalites have older Nd- and Hf-model ages ($T_{DM\ (Nd)}$ up to 1232 Ma) than the oldest ophiolite in the area (514–481 Ma; Jian

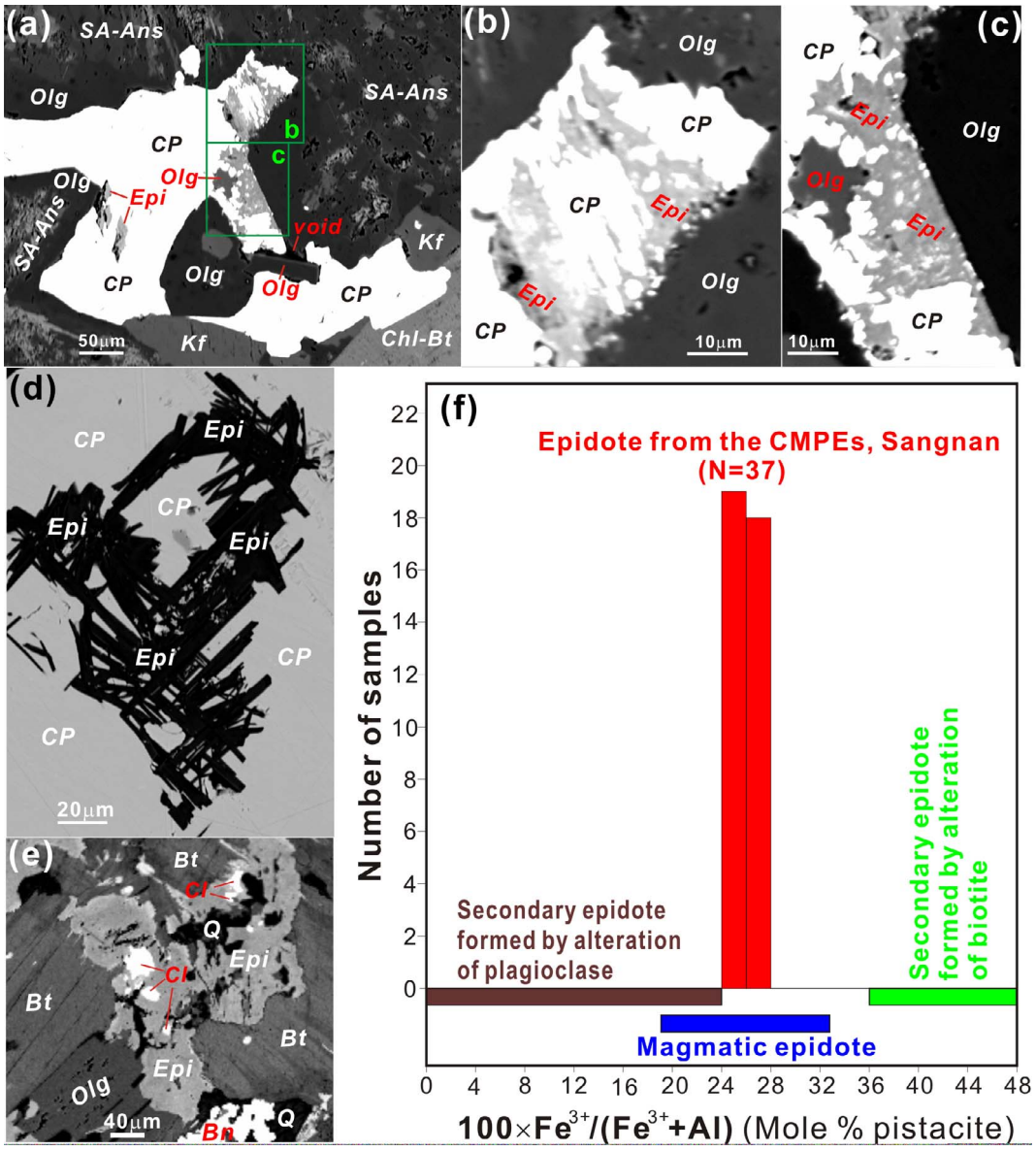


**Fig. 6.** Five back scattered electron images (a-e) showing the coexistence of chalcopyrite and epidote and a histogram of mol % Ps in epidote grains (f) in the CPMEs from the Sangnan area. Panel a with two enlargements b and c displays myrmekite-like chalcopyrite-epidote intergrowths and enclosure of epidote and oligoclase by chalcopyrite. Panel d shows a skeletal chalcopyrite-epidote intergrowth in a coarse chalcopyrite crystal. Panel e represents chalcopyrite inclusions (CI) in epidote. The compositional ranges of epidote from alteration of plagioclase and biotite are from Tulloch (1979), and magmatic epidote from Liou (1973), Zen and Hammarstrom (1984), Evans and Vance (1987), Dawes and Evans (1991), Owen (1991), Vyhnal et al. (1991), Farrow and Barr (1992), Sial et al. (1999) and Roberts et al. (2000). Bi: biotite, Bn: bornite, CP: chalcopyrite, CI: chalcopyrite inclusion, Ep: epidote, Kf: K-feldspar, Olg: oligoclase, SA-Ans: andesine with spongy texture and anhydrite alteration.

et al., 2003; Xiao et al., 2009; Zhang and Guo, 2010; Zeng et al., 2015; Liu et al., 2016) in East Junggar (Fig. 10c and d). Moreover, compared to adakites that were generated through fractional crystallization of parental arc basaltic magmas in Philippines (Castillo et al., 1999; Macpherson et al., 2006), most Sangnan tonalites have positive Eu/Eu* value. In addition, all the Sangnan tonalites have lower $Al_2O_3$ (< 16.05%) contents (Fig. 11), lower $(^{143}Nd/^{144}Nd)_i$ values (< 0.5125), Sr (< 500 ppm) and Rb (< 49 ppm), and higher Zr/Sm (> 40) than type adakites.

The positive Eu anomalies contained by the Sangnan tonalites indicate that these tonalite magmas probably had not undergone plagioclase fractionation. On the other hand, the Sangan tonalites have lower $(^{206}Pb/^{204}Pb)_i$ values (17.982–18.103) and plot in the field of the lower crust in $(^{207}Pb/^{204}Pb)_i$ versus $(^{206}Pb/^{204}Pb)_i$ diagrams (Fig. 10b), Nd-Hf isotope composition plots of the Sangnan tonalites are below the depleted mantle line (Fig. 10c) with a wider range of $T_{DM\ (Nd)}$, up to 1232 Ma. This indicates that older continental components from the lower crust most likely were involved with the adakitic tonalite melts at Sangnan (see DePaolo, 1981; Lesher, 1990). Correlation of major elements of the tonalites (Fig. 11) is very much the same as most adakitic rocks that were produced by partial melting of the lower crust in China, according to the data of Xu et al. (2002), Gao et al. (2004), Wang et al. (2005, 2006) and Jiang et al. (2007). Therefore, the Sangnan tonalites most likely owe their parentage to the partial melting of juvenile lower crust.

The CMPEs from the Sangnan tonalite pluton locally contain common features that are diagnostic of intruded blebs of mafic magma as follows:

(1) the CMPEs contain microgranular, elongated laths of zoned plagioclase, poikilitic K-feldspar and chalcopyrite, implying that the CMPEs were formed by quench crystallization of mafic magma

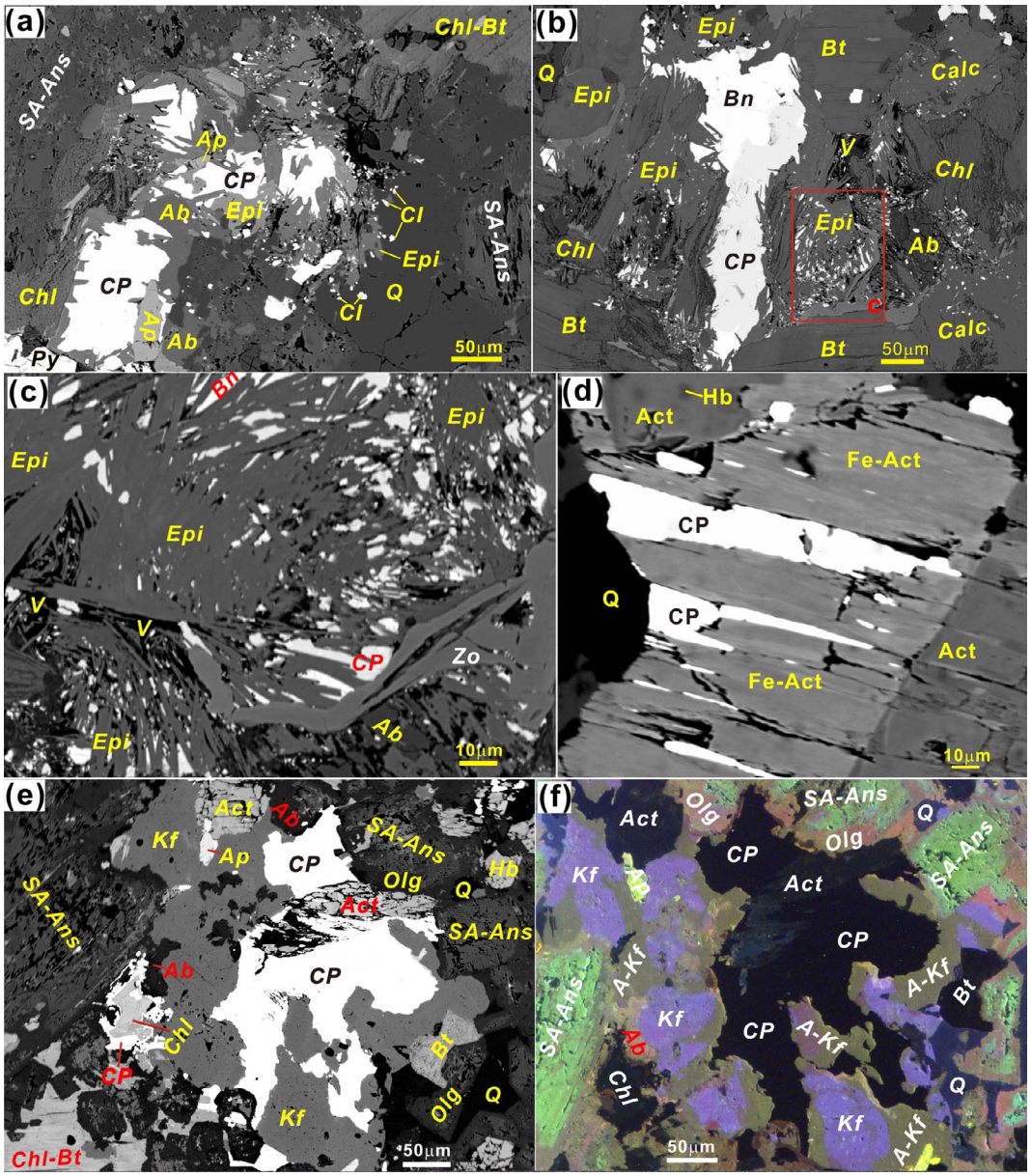


**Fig. 7.** Back scattered electron images showing feature and distribution of miarolitic Cu sulfide minerals (a, b and c) and chalcopyrite replacements of actinolite (d) and of K-feldspar (e) in the CMPEs from the Sangnan area. A CL panel (f) for a same domain with panel e was presented to show K-feldspar alteration induced by chalcopyrite replacement. Excepting images a and d from the thin section 6-3E and 6-4E respectively, the other panels are from the thin section 1-1E. Act: actinolite, Ans: andesine, Bn: bornite, Calc: calcite, Chl: chlorite, Bi: biotite, CP: chalcopyrite, CI: chalcopyrite inclusion, Ep: epidote, Fe-Act: ferro-actinolite, Kf: K-feldspar, Olg: oligoclase, Py: pyrite, Q: quartz, SA-Ans: andesine with spongy texture and anhydrite alteration, V: void, Zo: zoisite.

globules and blebs that were intruded into cooler granodioritic crystallizing magmas, which is similar to the process suggested by Didier and Barbarin (1991). Occurrence of needle-shaped zircons (Fig. 9c) and skeletal intergrowths of chalcopyrite and epidote (Fig. 6a and 7c) also demonstrate that such rapid cooling and crystallization of the CMPE magmas took place (e.g., Keller, 1988; London, 1996; Corfu et al., 2003; Vernon, 2004);

(2) development of overgrowths on groundmass oligoclase laths within the CMPEs on partial resorption surfaces of euhedral, medium-grained andesine in the host tonalite along contacts between the CMPEs and host tonalites (Fig.3c), suggest that the CMPE magmas were intruded into the tonalite with different compositions from that of the host tonalite. Close subsequent emplacement and similar formation depths of the CMPEs and their host tonalites suggest that the groundmass minerals of the CMPEs were crystallized at the same time and place as their host tonalite;

(3) and (3) the CMPEs are high-K calc-alkaline and belong to typical (normal) arc rocks with distinct geochemical signatures from their host tonalite, such as

(a) higher concentrations of oxides $TiO_2$, $Al_2O_3$, $TFe_2O_3$, MgO, CaO, $Na_2O$ and $K_2O$, S,
(b) higher concentrations of metals such as Cu, Nb, Sm, Y, and HREE,
(c) higher sum REE,
(d) lower Sr/Y value (Fig. 8b),
(e) negative Eu anomalies (Fig. 8d), and
(f) lower concentrations of Zr and higher concentrations of Nd (Fig. 8e).

The CMPEs do not have a direct link with their host tonalite plutons, and they are neither restites, autolith cumulates, nor are they concretionary enclaves (Didier and Barbarin, 1991). The absence of linear

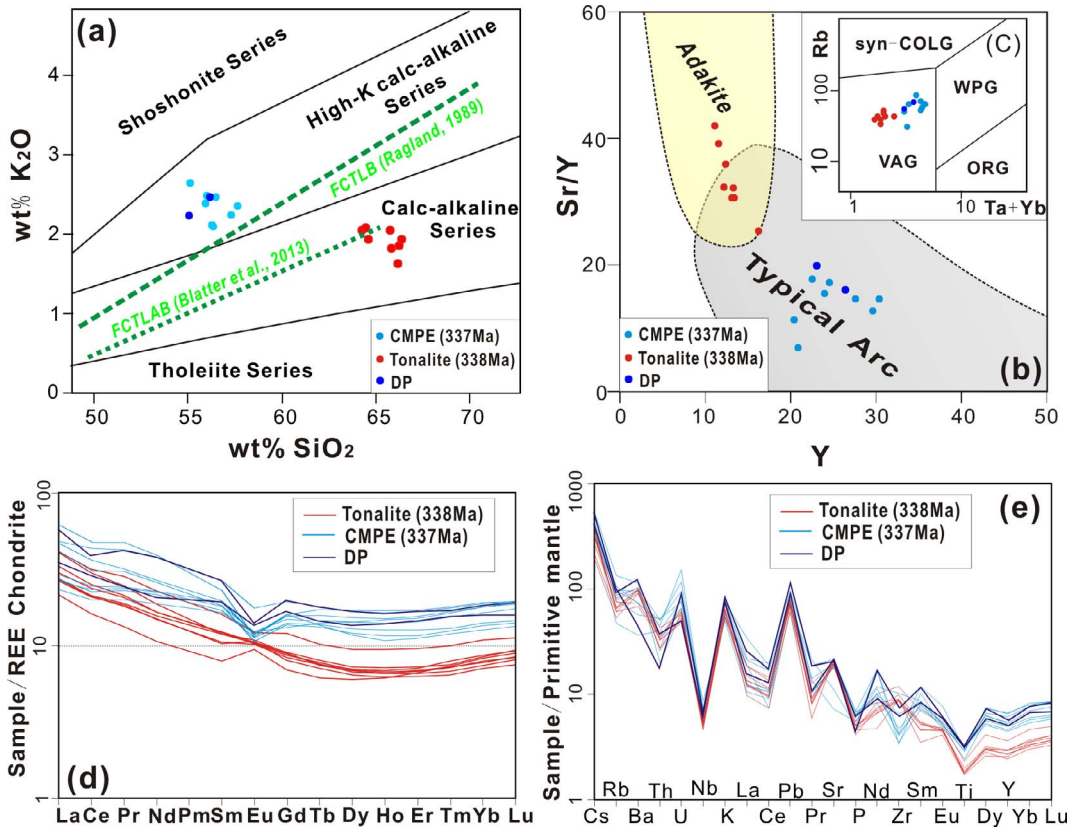


**Fig. 8.** (a) $SiO_2$-$K_2O$ diagram (after Peccerillo and Taylor, 1976), (b) Y versus Sr/Y diagram (after Defant and Drummond, 1990), (c) Rb versus Ta + Yb diagram (after Pearce et al., 1984), and (d) REE and (e) trace element spider diagrams for the CMPEs and their host tonalites from the Sangnan area. The fractional crystallization trend lines of basalt (FCTLB; Ragland, 1989) and arc basalt (FCTLAB; Blatter et al., 2013) were present in dashed and dotted green line in the panel a, respectively.

variation of bulk rock compositions between the CMPEs and their host tonalite excludes them from being hybrid magmas that were produced by magma mixing (Didier and Barbarin, 1991).

The CMPEs have accumulations of andesine phenocrysts and porphyritic textures that could be associated with a number of textural settings: (1) with intragranular microfractures and broken grain boundaries (Fig. 3e and f), (2) coarser angular magnetite that contains intragranular microfractures and corroded boundaries (Fig. 3 h) and (3) stubby zircon with corroded boundaries and overgrowth rims (Fig. 9e). This indicates that the CMPEs have textures that are typical of most porphyries, and that their phenocrysts were formed in a pre-emplacement chamber (Xu et al., 2009). The CMPEs also contain negative Eu anomalies, and have similar correlations between the content of total FeO (6.10–8.21 wt%) and MgO (3.16–4.58 wt%) with content of $SiO_2$ (55.09–57.66 wt%) to andesites that have been derived from fractional crystallization of hydrous basalt (Blatter et al., 2013). The CMPE sulfide minerals have similar sulfur isotopic compositions to rocks from the PCD at Bingham Canyon and to meteoritic sulfides (close to 0‰; Field, 1966; Hattori and Keith, 2001). Evidence that needle-shaped groundmass zircons and stubby phenocryst zircon both have broadly similar ages indicates that both these zircons cooled at same time. Therefore, these zircons were produced by the same magma in situ and in another pre-emplacement chamber. All these parameters strongly indicate that the CMPE magmas were dioritic magmas that were formed by fractional crystallization from parent basaltic magmas in a chamber below the host tonalite pluton in the Sangnan area.

The geochemistry of the rocks provides additional confirmation for the genesis of the CMPEs, the low Ni (5.28–10.76 ppm) concentrations of the CMPEs (Table 1) most likely resulted from prior fractional crystallization of olivine from the basaltic parental magmas. Association of magnetite and amphibole assemblage with plagioclase fractionation and accumulation indicates that the hypothetical parent basaltic magmas were oxidized and have high oxygen fugacity $fO_2$ (> ΔFMQ + 2.2) (Clemente et al., 2004). Because the needle-shaped zircons have higher weighted average $\varepsilon_{Hf(t)}$ (13.80) values than the stubby zircon phenocrysts ($\varepsilon_{Hf(t)}$ = 12.89), this indicates that the formation of groundmass magmas involved additional or continual feeding of juvenile mantle-derived melts. This feeding of mantle-derived melt was most likely the trigger for the uplift of the phenocryst-bearing magmas that were injected into the cooler granodioritic crystallizing tonalite magma chamber forming the CMPEs in the Sangnan area (Xu et al., 2009, 2016; Caricchi and Blundy, 2015). Additionally, the CMPEs have higher $K_2O$ (2.1–2.65%) content than those andesites that were produced by fractional crystallization of basalt (Ragland, 1989) and arc basalt (Blatter et al., 2013) at their silica content (Fig. 8a), implying that these CMPEs are anomalous in $K_2O$.

Additionally, the CMPEs have high Cu concentrations (2698–7128 ppm), and contain sulfides and other hydrothermal minerals within their central cores that are bounded by weakly altered or unaltered, fine-grained magnetite-oligoclase margins or carapaces. This indicates that the sulfide minerals are exclusive to the CMPEs, and therefore the Cu and ore fluids were most likely derived from CMPE magmas, and also that these small globules of magma (now CMPEs) were micro-closed systems of Cu-rich magmas. This conclusion is supported by the following evidence:

(1) the host tonalite contains relatively lower Cu concentrations (119–358 ppm), and are unaltered throughout, except for a few replacements in the narrow peripherals of the CMPEs. If the high-Cu concentrations of the CMPEs were related to external fluids, the host tonalite should also have high Cu concentrations and be accompanied by broad alternation zones that were not limited to the peripherals of the CMPE. If the tonalite had been the mineralizer, the Cu minerals would be in quartz veins. These hypothetical areas

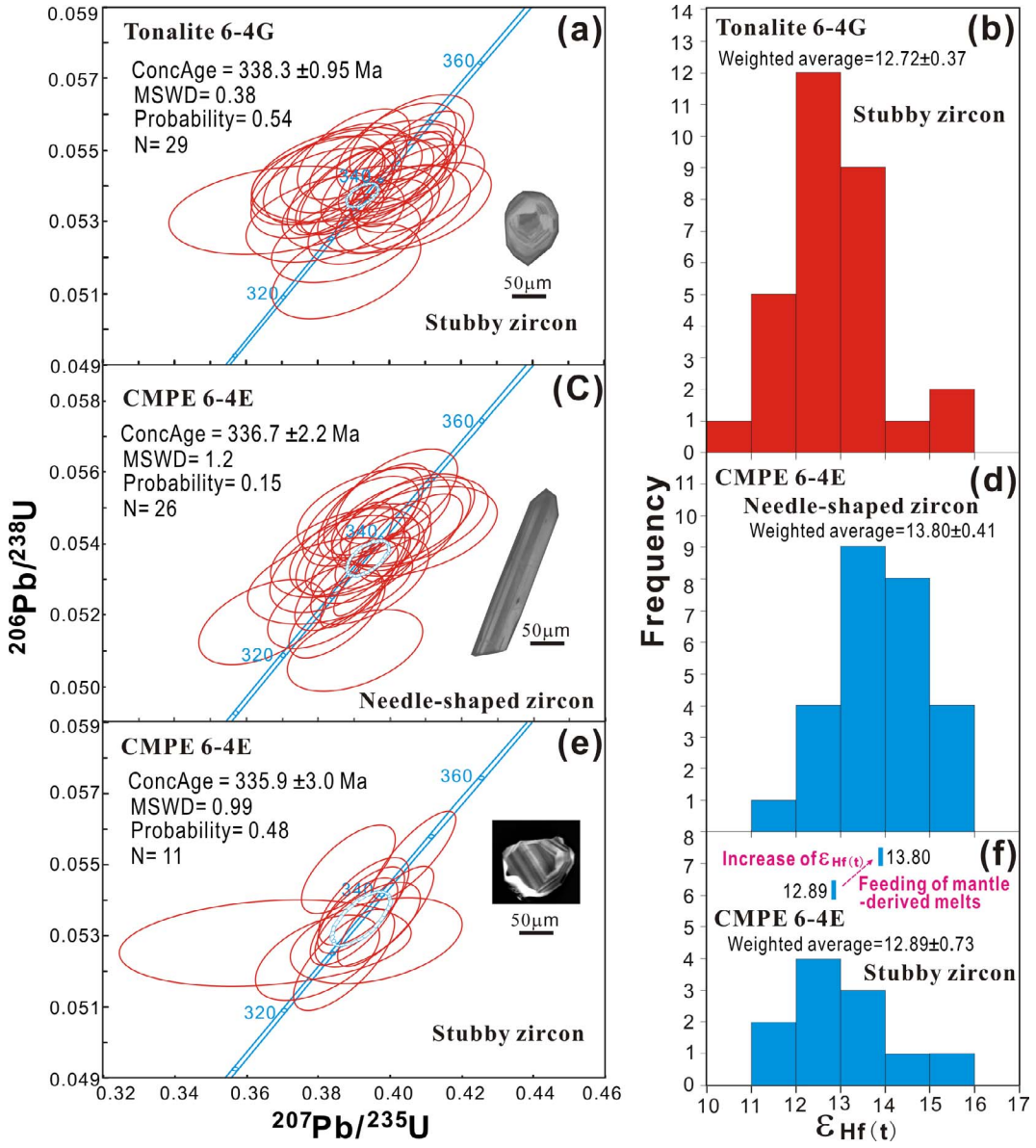


**Fig. 9.** Zircon SIMS U–Pb concordia age plots and frequency of $\varepsilon_{Hf(t)}$ for the CMPE 6-4E and its peripheral tonalite 6-4G from the Sangnan area. A cathodoluminescence image of the representative zircons is inserted in panels a, c and e.

not present in the host tonalite;

(2) most CMPE sulfide minerals are directly associated with magmatism of the CMPEs and are interstitial to silicate minerals, and some of them are directly intergrown with K-feldspar and quartz (Fig. 5b), whereas other sulfide minerals occur in miarolitic cavities (Fig. 7a and b);

(3) not only is there a spatial association of the sulfide minerals with the CMPEs, precipitation of the CMPE sulfide minerals closely followed the orderly crystallization of the groundmass oligoclase, apatite, K-feldspar, quartz and albite;

(4) occurrences of sulfide mineral-rich miarolitic cavities (Fig. 7a and b) implies Cu-rich magmatic fluids were derived from the CMPEs at late magmatic stage or at the magmatic-hydrothermal transition (see Harris et al., 2004); and

(5) the myrmekite-like and skeletal intergrowths of chalcopyrite and epidote demonstrate that some CMPE sulfide mineral clusters were formed in pegmatite-like systems during the late magmatic-hydrothermal stage (Shelley,1967; Fenn, 1986).

Formation of Cu-rich (1153–1227 ppm) dioritic porphyry magmas in the Sangnan area probably is similar to the CMPE magmas, because the dioritic porphyries have similar geochemical signatures to the CMPEs (Figs. 8, 10 and 11).@@

### 7.2. Origin of the CMPE and tonalite magmas

1) Origin of the tonalite magmas

The CMPEs were most likely formed in an arc setting because they contain enrichment in Pb, K and U, depletion in Nb, P and Ti (Fig. 8e), low Sr/Y (< 20) and high Y concentrations (> 20 ppm) (Fig. 8c; Pearce et al., 1984; Winter, 2001). They also have similar Nd-Sr-Pb-Hf isotope compositions to Ordovician-Devonian igneous rocks in the nearby Yemaquan magmatic arc (Fig. 10). This indicates that their parent basaltic magmas were derived from partial melting of a metasomatised mantle wedge. However, similar $(La/Yb)_N$ value (1.0–6.0) and similar Nd–Sr–Pb–Hf isotope composition imply a genetic link between the CMPE and the host tonalites. It is therefore suggested that the adakitic host tonalite magmas were formed by partial melting of mafic lower crust, which was triggered by the intrusion of hot basaltic magmas, with subsequent superficial intermixing (see Jiang et al., 2007;

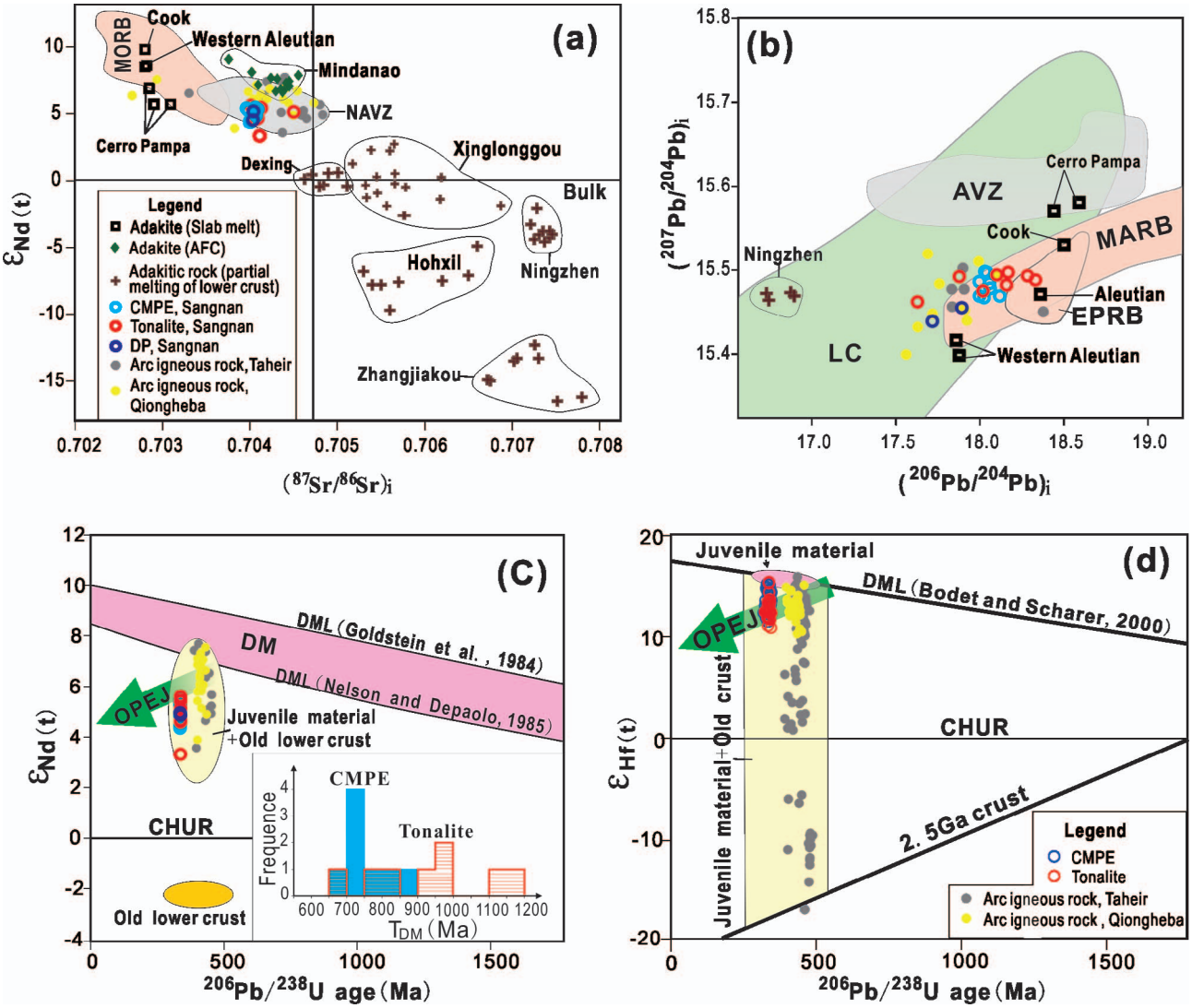


**Fig. 10.** $\varepsilon_{Nd(t)}$ versus $(^{87}Sr/^{86}Sr)_i$ (after Winter, 2001) (a), $(^{207}Pb/^{204}Pb)_i$ versus $(^{206}Pb/^{204}Pb)_i$ (after Zindler and Hart, 1986) (b), Nd isotope (b) and Hf isotope (d) plots of the CMPEs and their host tonalites from the Sangnan area. A panel of the $T_{DM}$ (Ma) frequency was inserted in panel c. The depleted mantle lines (DML) in the Nd diagram are after Goldstein et al. (1984) and Nelson and Depaolo (1985), and those in the Hf diagram are after Bodet and Scharer (2000). AVZ: Andean volcanic zone, AFC: assimilation and fractional crystallization; DM: depleted mantle, EPRB: Eastern Pacific Rise basalts; MARB: Mid-Atlantic ridge basalts, MORB: mid-ocean ridge basalts, NAVC: North Andean volcanic zone, LC: lower crust. Data of adakites and adakitic rocks are after Kay (1978), Kay et al. (1993), Schiano et al. (1995), Yogodzinski et al. (1995), Castillo et al. (1999), Xu et al. (2002), Gao et al. (2004), Wang et al. (2005, 2006), Macpherson et al. (2006) and Jiang et al. (2007)..

Richards and Kerrich, 2007). The high Cu concentration (119–358 ppm) of the host tonalite can be attributed to the high Cu content of the lower crust in the Qiongheba area and to incorporation of Cu from basaltic magmas. Occurrence of high Cr concentration (up to 96.94 ppm) in some tonalite demonstrates that this kind incorporation is most likely. Xu et al. (2002) reported that adakitic intrusive rocks have high Cu concentration, up to 291 ppm.

2) Origin of the CMPE magmas

Genesis of the CMPEs is likely due to complex processes as follows (Fig. 12):

(1) Formation of the oxidized basaltic magmas

The oxidized parent basaltic magmas inherited their oxidized states from the melting of a mantle wedge in the Sangnan area. Metasomatism by solute-rich hydrous fluids, such as water, $Fe^{3+}$ and K, originating from the subducting slab caused oxidization of mantle wedges (Parkinson and Arculus, 1999; Parkinson et al., 2003; Lee et al., 2005; Frost and McCammon, 2008). This leads to sulfide minerals in the mantle wedge were oxidized (Carroll and Rutherford, 1987; Jugo et al., 2005; Nadeau et al., 2010). This also increases of oxygen fugacity of basaltic melts (Thornber et al., 1980; Métrich and Clocchiatti, 1996; Tangeman et al., 2001; Ripley et al., 2002). Introduction of K caused the parent basaltic magmas and the CMPEs to have anomalously high K concentrations.

The oxidized basaltic magmas had greater capability to take in more sulfur and Cu from the mantle (e.g., Ripley and Brophy, 1995; Mavrogenes and O'Neill, 1999; O'Neill and Mavrogenes, 2002; Ripley et al., 2002; Jugo et al., 2005, 2009. 2010; Wallace and Edmonds, 2011). Since solubility of sulfur is strongly dependent on potassium concentration (Métrich and Clocchiatti, 1996), high-potassium basaltic melts would have high sulfur content. On the other hand, higher dissolved S in the basaltic melts may enhance the solubility of metals in the melt (Jego et al. 2010; Wallace and Edmonds, 2011). All these processes allow the parent basaltic magmas of the enclave magmas to become more fertile. Lee et al. (2012) suggested that the basaltic magmas with high oxygen fugacity $fO_2$, two orders of magnitude higher than the fayalite–magnetite–quartz oxygen buffer (ΔFMQ + 2) could contain approximately 330 ppm Cu. Crystallization of phenocryst magnetite indicates that the parent basaltic magmas of the enclave magmas

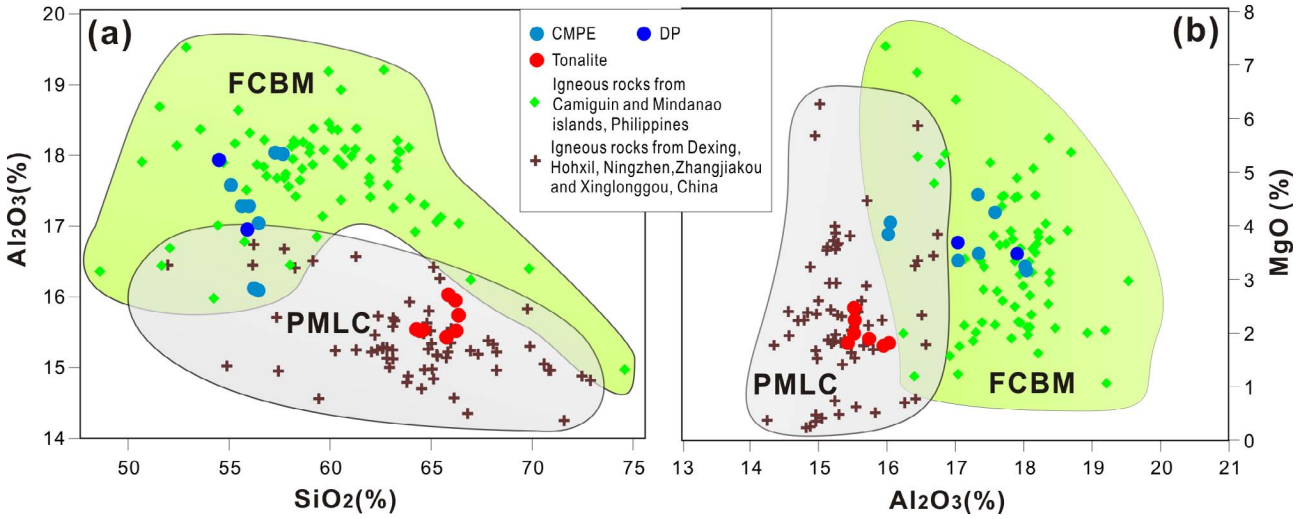


**Fig. 11.** $SiO_2$-$Al_2O_3$ (a) and $Al_2O_3$-MgO (b) diagram of the CMPEs and their host tonalites from the Sangnan area. Plots of igneous rocks produced by fractional crystallization of basaltic magmas in Philippines (Castillo et al., 1999; Macpherson et al., 2006) and by partial melting of lower crusts in China (Xu et al., 2002; Gao et al., 2004; Wang et al., 2005, 2006; Jiang et al., 2007) were present for comparison.

have high oxygen fugacity $fO_2$ (> ΔFMQ + 2.2) (Clemente et al., 2004), implying that the fertile parent basaltic magmas could have had Cu content > 330 ppm.

(2) Absorption, fractional crystallization and formation of Cu-rich magma

Blatter et al. (2013) reported that crystallization of oxidized, moderately hydrous arc basalt at mid to lower-crustal pressures to form andesitic magmas went thorough three stages: clinopyroxenite, pyroxene gabbro and hornblende gabbro. For runs at 900 MPa and 1200–950 °C, crystallization of magnetite and plagioclase occurred at 1035–975 °C at pyroxene gabbro stage. Occurrence of magnetite phenocrysts and andesine accumulations in the enclave magmas documents that the parent basaltic magmas would have undergone thorough fractional crystallization at pyroxene gabbro phase at a pressure of 9 kbar as well (Blatter et al., 2013). Luhr and Carmichael (1985) suggested that pyroxene accumulation usually occurs at the transitional zone between lower-crustal and upper-mantle, and this is also where Cu sulfide minerals were cumulated in a normal arc (Lee et al., 2012; Chiaradia, 2014). This means that the fractional crystallization of the fertile basaltic magmas probably took place in a subcrustal chamber. This chamber most likely was located between the lower-crust and upper-mantle at a depth of approximately 30 km, in which some accumulated Cu sulfide minerals were absorbed by the oxidized basaltic magmas and thereby increased the overall concentration of sulfur and Cu in the melts.

Fractional crystallization of basaltic magmas led to enrichment of ferric ion ($Fe^{3+}$), $K_2O$, $Na_2O$, $Al_2O_3$, CaO, $H_2O$, $P_2O_5$ and Cu in the residual melts, and a depletion of Ni concentration (e.g., Luhr and Carmichael, 1985; Christie and Carmichael, 1986; Ragland, 1989; Carmichael, 1991; Wallace and Gerlach, 1994; Métrich et al., 2001; Wallace, 2005; Johnson et al., 2008, 2010; Lee et al., 2010). Higher

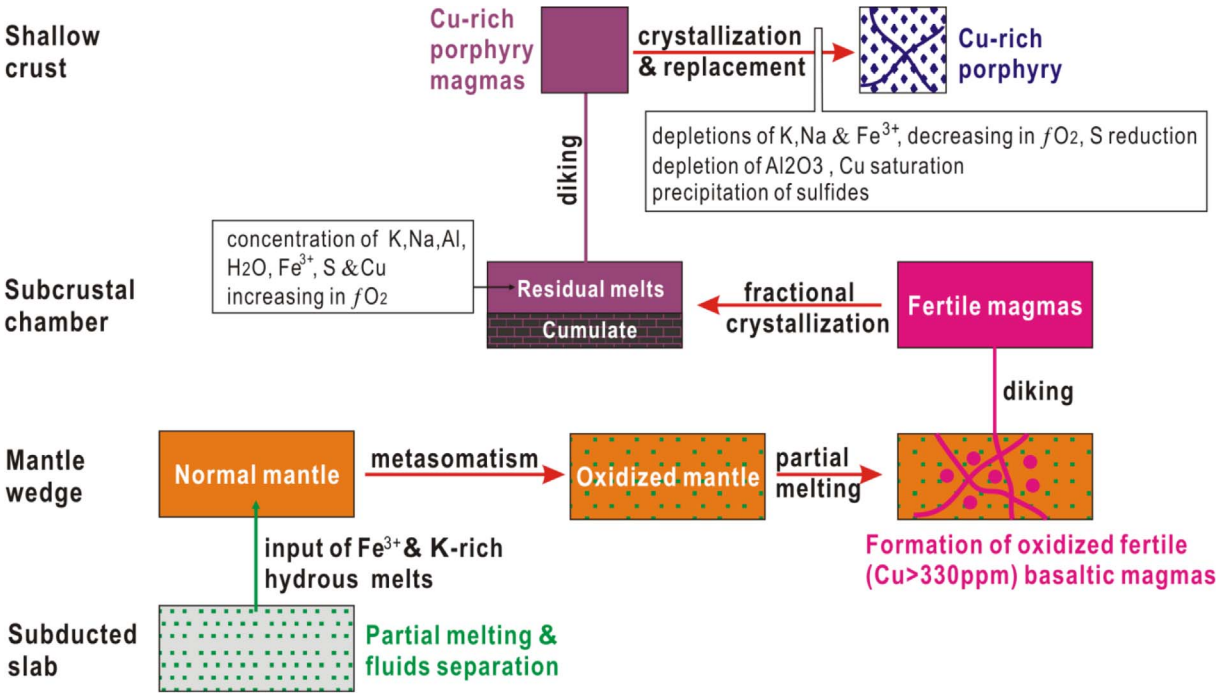


**Fig. 12.** A schematic diagram showing formation processes of fertile basaltic and Cu-rich porphyry magmas.

concentration of $Fe^{3+}$ and enrichment of K and Na further increased the oxygen fugacity $fO_2$ of the residual melts, and allowed these residual melts to dissolve more sulfur. The enrichment of $Al_2O_3$ and CaO also enhanced the solubility of Cu in the residual melts (Ripley et al., 2002). Because increased S in the residual melts raised the solubility of Cu in the melts, this allowed further concentration of Cu during fractional differentiation processes (Jego et al. 2010; Wallace and Edmonds, 2011).

Lee et al. (2012) showed that fractional crystallization could increase oxygen fugacity $fO_2$ of basaltic magmas from ΔFMQ to ΔFMQ + 1.3 with Cu concentration of from 70 ppm to near 200 ppm in models. Additionally, some pyroxenite cumulates in these melts created during fractional crystallization have high Cu concentrations (> 400 ppm). This means that fractional crystallization of basaltic magmas concentrates Cu nearly three to six times. However, this kind Cu concentration by fractional crystallization is still less than the Cu concentration in the CMPEs, and other processes are therefore necessary to increase Cu content (Hedenquist and Lowenstern, 1994). It is suggested that the pre-existed Cu or Fe-Cu sulfide cumulates at transitional zone between lower-crustal and upper-mantle (Core et al., 2006; Lee et al., 2012; Chiaradia, 2014) were required to participate in the Cu enrichment for the CMPE magmas in order to achieve the higher Cu concentrations. This suggestion is demonstrated by the occurrence of fractured magnetite phenocrysts, some of which were possibly formed during absorption of sulfide cumulates. The absorption is thought to have taken place before fractional crystallization.

3) Tectonic setting for the CMPEs and their host tonalites

Xu et al., 2013b suggested that the East Junggar terrane was related to the southward subduction of the Paleo-Asian oceanic plate beneath the Junggar continent along the Armantai area in the early Paleozoic and shifted to intra-oceanic subduction along the Erqis area at middle Devonian. The Junggar oceanic plate provides a back-arc ocean basin. Recently, Hong et al. (2015, 2017) demonstrated that the final closure of the Paleo-Asian Ocean along the Erqis ophiolite belt and the collision between the Sawuer island arc and Altay terrane occurred at approximately 360 Ma. Xu et al. (2015) reported that the Zhifang ophiolites contain segments of the 371 Ma MORB-type layered rocks and 363 Ma oceanic islands, and therefore the Junggar Ocean in the Zhifang area most likely closed at approximately 343 Ma. In this tectonic scenario, the late Carboniferous (338–337 Ma) arc-type CMPEs and their host tonalites were most likely related to northward subduction of the young Junggar ocean plate (Fig. 13). Closure of the Junggar Ocean in the Daheishan area should be later than that in the Zhifang area.

4) Formation model of the CMPE and tonalite magmas

Formation mechanism of the CMPE and tonalite magmas was summarized as follows (Figs. 13, 14):

(1) In late Carboniferous (338–337 Ma), the Qiongheba mantle wedge was metasomatized and partially melted to produce oxidized basaltic magmas, which was caused by introduction of high-water melts from the subducting slab of the Junggar Oceanic lithosphere. The oxidized basaltic magmas incorporated > 330 ppm Cu from the mantle.
(2) These basaltic magmas were emplaced in a subcrustal chamber at a transition zone between the lower-crust and upper-mantle.
(3) The adakitic tonalite magmas were formed by partial melting of mafic lower crust, which was triggered by the intrusion of hot basaltic magmas, with subsequent assimilation and Cu incorporation. The adakitic tonalite magmas were emplaced in an intermediate magma chamber at middle crustal level.
(4) Absorption of former sulfide-rich cumulates and fractional crystallization of the fertile basaltic magmas in the subcrustal chamber produced Cu-rich andesitic residual magmas, some of which intruded into the crystallizing adakitic tonalite magma chamber to form the CMPEs as well as some dioritic porphyries in the Sangnan area.
(5) These Cu-rich residual magmas may have been transported and emplaced to a shallow level to form Cu porphyry magmas and subsequently deposits (Xu et al., 2012). The Cu-Zn albite porphyry dikes in the Hersai deposit in the Qiongheba area, East Junggar are another case of this kind magma (Xu et al., 2014).

### 7.3. Mineralization of the CMPEs

Evidence that the chalcopyrite and pyrite are dominantly disseminated as discrete or interstitial grains within the groundmass and their host CMPEs have porphyritic texture (Figs. 3d, f and 5) indicates that the CMPEs in the tonalite pluton of the Qiongheba area, East Junggar have some mineralization features of PCDs (Lowell and Guilbert, 1970; Titley and Beane, 1981; Seedorff et al., 2005; Hedenquist and Lowenstern, 1994; Harris et al., 2004; Cooke et al., 2005). The CMPE sulfide minerals were precipitated in sulfide-rich porphyry Cu systems during late magmatic-hydrothermal stages because:

(1) intergrowths of chalcopyrite and groundmass oligoclase, K-feldspar and quartz in the CPMEs (Figs. 3d and 5b) indicate that formation of sulfide minerals began during a late magmatic stage (Zavaritsky, 1927);
(2) the albites occur along the walls of the intergranular spaces and were closely followed by interstitial poikilitic chalcopyrite grains that contain inclusions of hornblende, oligoclase, K-feldspar,

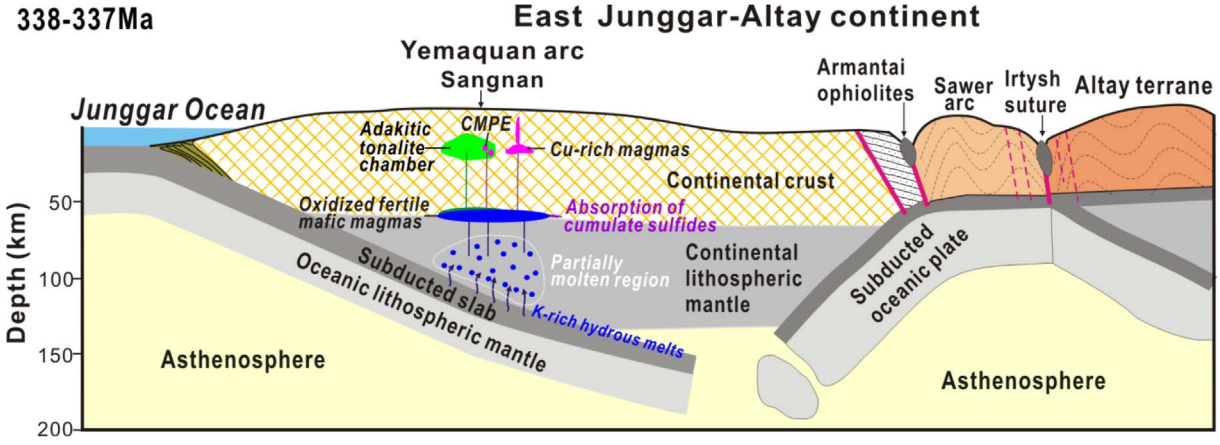


**Fig. 13.** Tectonic setting model for the CMPEs and their host tonalites in the Sangnan area.

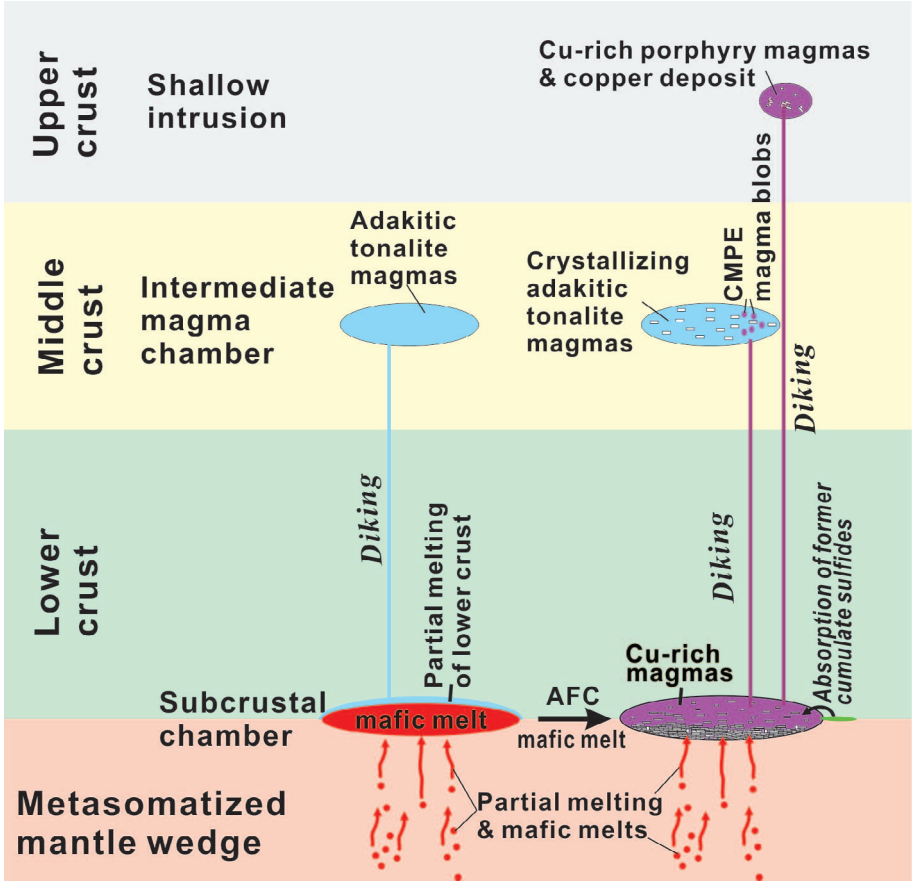


**Fig. 14.** Formation model for the CMPEs and their host tonalites in the Sangnan area. AFC: assimilation and fractional crystallization.

oligoclase, apatite and epidote. Sienna luminescing in albite minerals (Fig. 5d and 6a) suggests that albite and subsequent chalcopyrite were precipitated along a transition zone that define late magmatic and hydrothermal events. Because magmatic albite usually is bright orange, red or blue luminescent (e.g., Dalby et al., 2010; Götze, 2012; Xu et al., 2014), hydrothermal albite is non-luminescent (Yu et al., 1997; Finch and Klein, 1999);

(3) occurrences of sulfide-rich miarolitic cavities (Fig. 7a and b) also indicate that some Cu sulfide minerals were formed along the magmatic- hydrothermal transition (Harris et al., 2004);

(4) developments of skeletal intergrowths of chalcopyrite and epidote indicate that the CMPE sulfide minerals were formed in pegmatite-like systems, which were supersaturated in sulfide and epidote components (Shelley,1967; Fenn, 1986). Nature of sulfide supersaturation was also documented by small volume content of voids that are much less than volume content of sulfide minerals in the CMPEs. Solubility of Cu sulfide minerals, both in vapor phases and in hydrothermal fluids is < 5 wt% in natural and experimental conditions (e.g., Crerar and Barnes, 1976; Heinrich et al., 1992; Hemley et al., 1992; Ulrich, 2002; Baker et al., 2004). Precipitation of Cu sulfide minerals from hydrothermal fluids requires a greater quantity of fluids that should be twenty times greater than the Cu sulfide minerals in weight; and

(5) association of some chalcopyrite with hydrothermal minerals (actinolite, chlorite and calcite quartz; Fig. 7d and e) in the CMPEs suggests that precipitation of the sulfide minerals in the CMPE were temporally associated with hydrothermal mineralization (Richards, 2011). Myrmekite-like intergrowths of chalcopyrite and epidote were likely formed by metasomatism during the hydrothermal stage as well (Shelley, 1967). Therefore, the CMPEs underwent late magmatic-hydrothermal mineralization, and the CMPE ore fluids are magmatic and sulfide-rich.

Mineralization of the CMPEs involves three stages: (1) growth of phenocryst magnetite in the subcrustal basaltic chamber subjacent to the tonalite chamber, (2) crystallization of groundmass magnetite and finally (3) Cu-Fe sulfide minerals in the CMPEs in the tonalite chamber. The groundmass magnetite is mainly distributed along the margins of the CMPEs, whereas the Cu-Fe sulfide minerals are commonly located within the cores of the CMPEs. The occurrence of magnetite inclusions in the oligoclase rims of phenocryst andesine (Fig. 3d) indicates that the groundmass magnetite possibly crystallized before oligoclase. Precipitation of the CMPE sulfides began at a late magmatic stage and went through a hydrothermal stage.

Precipitation of the CMPE sulfides were affected and controlled by crystallization of silicate minerals and oxides. As mentioned above, solubility of sulfur and metal is strongly influenced by oxygen fugacity, composition and temperature. Crystallization of $Fe^{3+}$-bearing mineral such as groundmass magnetite, hornblende and biotite in the CMPEs could cause depletion of the melt in $Fe^{3+}$ with decreasing oxygen fugacity and shifting of redox states from oxidized to reductive (Fig. 12; Carmichael and Ghiorso, 1986; Bacon, 1989; Carmichael, 1991; Sun et al., 2004), resulting in decreasing sulfur solubility and changing sulfur species in the melts (e.g., Carroll and Rutherford, 1985, 1988; Mavrogenes and O'Neill, 1999; Clemente et al., 2004; Behrens and Gaillard, 2006; Jugo et al., 2005, 2010; Jugo, 2009; Wallace and Edmonds, 2011). For example, crystallization of magnetite could cause sulfate to be reduced by the reaction (Carmichael and Ghiorso, 1986; Jenner et al., 2010):

$$FeO + SO_4^{2-} \rightarrow Fe_3O_4 + S^{2-} \quad (1)$$

Crystallization of potassium and sodium minerals, such as K-feldspar and albite in the CMPEs, could cause depletion in potassium and sodium in the melts and fluids (Fig. 12). The charge-balancing role of alkali cations would disappear, and $Fe^{3+}/Fe^{2+}$ ratios and oxygen

fugacity decrease (Métrich and Clocchiatti, 1996; Tangeman et al., 2001). These processes would force both sulfur bearing phases out of their stability field and drive sulfur out of the magma or fluids, resulting closely association of sulfide with potassium and sodium minerals. This is possibly the genesis that most Cu and Fe sulfides deposited closely following with K-feldspar and albite in the CMPEs. It is possibly also the reason that sulfides are usually closely and subsequent association with potassium minerals, i.e. K-feldspar, biotite and muscovite, in PCDs around the world (e.g., Cooke et al., 2005; Seedorff et al., 2005; Zajacz et al., 2010).

Similarly, crystallization of epidote would cause last depletion in $Al_2O_3$ and CaO in the melts and fluids, resulting in saturation and crystallization of Cu sulfides (Ripley et al., 2002). This leads to intergrowths of chalcopyrite and bornite with epidote crystals in the CMPEs (Fig. 7b).

Additionally, temperature decreasing at late magmatic stage, such as below 750 °C, could decrease the solubility of sulfur in melts (Wendlandt, 1982; Carroll and Rutherford, 1987; Wallace and Gerlach, 1994; Wallace, 2005) and enhance saturation of sulfur and precipitation of sulfides.

Replacement of andesine by anhydrite in the CMPEs indicates that reduction of sulfur oxide was possibly related to chemisorption reaction at temperature above 400 °C (Henley et al., 2015) by the reaction:

$$3CaAl_2Si_2O_8 + 4SO_2(g) + H_2O(g) \rightarrow 3CaSO_4 + 3Al_2SiO_5 + 3SiO_2 + H_2S \quad (2)$$

At ≤400 °C reduction of sulfur oxide in the CMPEs was possibly related to disproportionation of $SO_2$, which allowed conversion of magmatic $SO_2$ to aqueous sulfate and $H_2S$ at hydrothermal mineralization stage by the reaction (Ohmoto and Lasaga, 1982),

$$4SO_2 + 4H_2O = 3H_2SO_4 + H_2S \quad (3)$$

The $S^{2-}$ and $H_2S$ generated by above ways provide sulfide ions for sulfide precipitation (Simon and Ripley, 2011). The $H_2SO_4$ leads to extreme base leaching and the formation of vuggy texture and acid-sulfate alteration (Hedenquist and Lowenstern, 1994).

Cu dissolution in melts is generally present in the form of monovalent (e.g., Ripley and Brophy, 1995; Lee et al., 2012). The valence state of Cu is also affected by content of alkali composition (Holzheid and Lodders, 2001). Alkali element ions (e.g., $K^+$) can combine with $Fe^{3+}$ ions to form $(FeK)^{4+}$ polycations in silicate melts with high basicity (e.g., Turkdogan, 1983). This causes the $Fe^{3+}/Fe^{2+}$ ratio to increase in the silicate melt. Higher $Fe^{3+}$ concentrations then move the redox equilibrium $Cu^+ + Fe^{3+} = Fe^{2+} + Cu^{2+}$ toward larger amounts of $Cu^{2+}$ in the melt. Such a reaction may account for the correlation of higher formal Cu valences with higher alkali element content (Holzheid and Lodders, 2001). However, crystallization both of ferric-bearing mineral (magnetite and hornblende) and alkalic feldspar (K-feldspar and Na-feldspar) could cause depletion in $Fe^{3+}$, then move the redox equilibrium in reverse to form monovalent Cu in the melt and fluids, resulting in concentration of monovalent Cu. On the other hands, the valence state of Cu in chalcopyrite is bivalent, this require most monovalent Cu should be changed to bivalent Cu during precipitation of chalcopyrite in the CMPEs. Here, it is proposed that oxidization of Cu from monovalent to bivalent may cause reduction of sulfur oxide by a reaction:

$$Cu^+ + SO_2 + H^+ \rightarrow Cu^{2+} + S^{2-} + H_2O \quad (4)$$

Absence of coexistence of sulfides with groundmass magnetite in the CMPEs indicates that crystallization of the groundmass magnetite could cause sulfates to be reduced, but had not driven precipitation of sulfides. Both the reactions (2) and (3) will produce a great number of associated sulfates, such as alunite in an open epithermal system and possibly anhydrite in a hypogene system, with a content of three times of coeval sulfides. Evidence that content of sulfide in the CMPEs is much more than that of anhydrite suggests that the new reaction (4) is possibly a main reduction mechanism for the CMPE sulfides rather than the chemisorption reaction (Henley et al., 2015) and disproportionation of $SO_2$ (Ohmoto and Lasaga, 1982) mechanism.

In summary, the CMPEs contain mineralization geochemically and mineralogically similar some PCDs and they also contain abundant disseminated sulfide minerals and some typical PCD hydrothermal alteration. Sulfur oxide may be reduced in the CMPEs by oxidization of Cu from monovalent to bivalent.

## 8. Conclusions

The CMPEs in the tonalite pluton in the Sangnan area, East Junggar have porphyritic textures, and contain accumulated phenocrysts and disseminated interstitial sulfide minerals. The CMPEs probably represent globules of Cu-rich porphyry magmas, which were produced by fractional crystallization of oxidized fertile basaltic magmas in a subcrustal chamber separate from the tonalite chambers. High Cu-concentrations of the parent basaltic magmas in the Sangnan area were mainly derived from metasomatised mantle wedges, and by additional absorption of sulfide-rich cumulates in the lower crust.

## Acknowledgements

This research was jointly supported by the NSFC (Grant number 41390442 and 41072060), the National 305 Project (Grant number 2011BAB06B03-3 and 2006BAB07B01-03) and the CAS Knowledge Innovation Project (Grant number kzcx-ew-ly03 and kzcx2-yw-107). We would like to thank Jin-Wen Mao, Guang-Ming Li, Xiao-Hui Zhang, Jing-Xiang Li and Jeremy P. Richards for valuable discussions, and Steve Ludington for a review on a manuscript of this contribution. This paper was significantly improved by the thorough and incisive review of Franco Pirajno, Ibrahim Uysal and two anonymous reviewers.

## APPENDIX B

### *Analytical techniques*

Internal textures and structures of the CMPEs were analyzed by optical cathodoluminescence (optical-CL) microscopy and by back-scattered electron (BSE) images that were produced by an electron microprobe. The optical-CL microscope consists of a LV100 POL with a DS camera DS-Ri1 (Nikon, Japan) and a Reliotron III stage (Relion, USA). The Reliotron III stage has a cold cathode electron gun that bombards the surface of well-polished thin sections with an electron beam in a moderately-high vacuum. Beam voltage and beam current during analysis were 4–8 kV and 0.3–0.5 mA, respectively.

For geochemical analyses, hand specimens were crushed in a tungsten carbide swing mill, sieved, ultrasonically cleaned several times in deionized water and then ground in an agate mortar. Rock powders (~1.2 g) were then dissolved with $Li_2B_4O_7$ ( g) in a TR-1000 S automatic bead fusion furnace at 1100 °C for 10 min. Major element abundances (wt%) were determined on whole-rock powder pellets by X-ray fluorescence (XRF) using an XRF-1500 sequential spectrometer made by Shimadzu Corporation, Japan. Analytical uncertainties are 1–3% for major elements. Loss on ignition was obtained by weighing after 1 h of calcinations at 1100 °C. For rare earth element (REE) and trace element analyses, rock powders (50 mg) were dissolved using a mixed acid (HF:HClO4 = 3:1) in capped Savillex Teflon beakers at 120 °C for 6 days, and subsequently dried to wet salt and redissolved in 0.5 ml $HClO_4$. The solutions were then evaporated to wet salt at 140 °C and redissolved in 1 ml $HNO_3$ and 3 ml water for cr. 24 h at 120 °C. The solutions were diluted in 2% $HNO_3$ for analysis. REE and trace element concentrations were determined by inductively coupled plasma mass spectrometry (ICP–MS) using a PQ2 Turbo system. Uncertainties based on repeated analyses of internal standards are ± 5% for REE and ± 5–10% for trace elements.

Compositions of minerals from the 16 thin sections were analyzed using a CAMECA SX51 electron microprobe at IGGCAS. The accelerating voltage was 21 kV and the sample current was 10 nA. Beam diameters were 10 μm for mineral crystals of the tonalite and phenocryst minerals of the CPMEs, 5 μm for groundmass minerals of the CPMEs, and 2 μm for epidote crystals that are intergrown with chalcopyrite or contain exsolution of chalcopyrite in the CPMEs. The counting times for all elements were 10 s. Well defined natural minerals were used as standards. All the 16 thin sections of the selected samples were observed using a CAMECA SX51 electron microprobe.

Samples for isotopic analysis were dissolved in Teflon bombs after being spiked with $^{84}Sr$, $^{87}Rb$, $^{150}Nd$ and $^{147}Sm$ tracers prior to HF + $HNO_3$ (with a ratio of 2: 1) dissolution. Rb, Sr, Sm and Nd were separated using conventional ion exchange procedures and measured using a Finnigan MAT 262 multi-collector mass spectrometer. Procedural blanks were < 100 pg for Sm and Nd and < 500 pg for Rb and Sr. $^{143}Nd/^{144}Nd$ were corrected for mass fractionation by normalization to $^{146}Nd/^{144}Nd = 0.7219$, and $^{87}Sr/^{86}Sr$ ratios were normalized to $^{86}Sr/^{88}Sr = 0.1194$. Typical within-run precision (2σ) for Sr and Nd was estimated to be ± 0.000015. The measured values for the La Jolla and BCR-1 Nd standards and the NBS-607 Sr standard were $^{143}Nd/^{144}Nd = 0.511853 \pm 7$ ($2\sigma_n$, n = 3) and $0.512604 \pm 7$ ($2\sigma_n$, n = 3), respectively, and $^{87}Sr/^{86}Sr = 1.20042 \pm 2$ ($2\sigma_n$, n = 12) during the period of data acquisition.

Zircon grains were separated using conventional heavy fraction and magnetic techniques. Representative zircon grains, together with zircon standard Qinghu (159.5 Ma, Li et al., 2013) and standard 91,500 (1065 Ma, Wiedenbeck et al., 1995), were mounted in epoxy mounts which were then polished section that contained crystals in half for analysis. All mounted zircon grains were documented with transmitted and reflected light micrographs as well as cathodoluminescence (CL) images to reveal their internal structures. Following the CL and other imaging, the samples were vacuum-coated with high-purity gold.

Measurements of U, Th and Pb were conducted using the Cameca IMS–1280 SIMS. U–Th–Pb ratios and absolute abundances were determined relative to the standard zircon 91500 (Wiedenbeck et al., 1995), analyses of which were interspersed with those of unknown grains, using operating and data processing procedures similar to those described by Li et al. (2009). A long-term uncertainty of 1.5% (1 RSD) for $^{206}Pb/^{238}U$ measurements of the standard zircons was propagated to the unknowns, despite that the measured $^{206}Pb/^{238}U$ error in a specific session is generally around 1% (1 RSD) or less. Measured compositions were corrected for common Pb using non-radiogenic $^{204}Pb$. Corrections are sufficiently small to be insensitive to the choice of common Pb composition, and an average of present-day crustal composition (Stacey and Kramers, 1975) is used for the common Pb assuming that the common Pb is largely surface contamination introduced during sample preparation. Uncertainties on individual analyses in data tables are reported at a 1σ level; mean ages for pooled U/Pb (and Pb/Pb) analyses are quoted with 95% confidence interval. Data reduction was carried out using the Isoplot/Ex v. 2.49 programs (Ludwig, 2001).

In situ zircon Lu–Hf isotopic analyses were carried out using a Neptune MC–ICPMS with an ArF excimer laser ablation system. Hf isotopic analyses were obtained on the same zircon grains that were previously analyzed for U–Pb isotopes, with ablation pits of 40 μm in diameter, and a laser repetition rate of 10 Hz with 100 mJ were used. Details of the technique are described by Wu et al. (2006). During analyses, the $^{176}Hf/^{177}Hf$ and $^{176}Lu/^{177}Hf$ ratios of standard zircon (91,500) were $0.282294 \pm 15$ ($2\sigma_n$, n = 20) and 0.00031, similar to the commonly accepted $^{176}Hf/^{177}Hf$ ratio of $0.282284 \pm 3$ (1σ) measured using the solution method (Goolaerts et al., 2004; Woodhead et al., 2004).

The separated sulfide minerals were crushed to 200 mesh. Fifteen mg of the material was taken from each powered sample and mixed with Cu oxide powder. The mixture was reacted in an oven at 1100 °C for 15 min to extract $SO_2$. The sulfur isotopic compositions of the extracted $SO_2$ were determined on a Finnigan-Mat 252 ratio mass spectrometer at the IGGCAS. The $^{34}S/^{32}S$ ratios are expressed by the conventional $\delta^{34}S$ value in ‰ relative to CDT. The reproducibilities of the $\delta^{34}S$ values are ± 0.2‰.

## Appendix B. Supplementary data

Supplementary data associated with this article can be found, in the online version, at http://dx.doi.org/10.1016/j.oregeorev.2017.09.020.

## References


Audétat, A., Pettke, T., 2006. Evolution of a porphyry-cu mineralized magma system at santa rita, New Mexico (USA). J. Petrol. 47, 2021–2046.

Bacon, C.R., 1989. Crystallization of accessory phases in magmas by local saturation adjacent to phenocrysts. Geochim. Cosmochim. Acta 53, 1055–1066.

Baker, T., Van Achterberg, E., Ryan, C.G., Lang, J.R., 2004. Composition and evolution of ore fluids in a magmatic-hydrothermal skarn deposit. Geology 32, 117–120.

Behrens, H., Gaillard, F., 2006. Geochemical aspects of melts: volatiles and redox behavior. Elements 2, 275–280.

Blatter, D.L., Sisson, T.W., Hankins, W.B., 2013. Crystallization of oxidized, moderately hydrous arc basalt at mid to lower-crustal pressures: implications for andesite genesis. Contrib. Miner. Petrol. 166, 861–886.

Bodet, F., Scharer, U., 2000. Evolution of the SE-Asian continent from U-Pb and Hf isotopes in single grains of zircon and baddeleyite from large rivers. Geochim. Cosmochim. Acta 64, 2067–2091.

Candela, P.A., Holland, H.D., 1986. A mass transfer model for copper and molybdenum in magmatic hydrothermal systems: the origin of porphyry-type ore deposits. Econ. Geol. 81, 1–19.

Caricchi, L., Blundy, J.D., 2015. Temporal Evolution of chemical and Physical properties of magmatic systems. In Caricchi, L. and Blundy, J.D. (eds) Chemical, physical and temporal evolution of magmatic systems. Geological Society, London, Special Publications, 422, doi: 10.1144/SP422.11.

Carmichael, I.S.E., 1991. The redox states of basic and silicic magmas: a reflection of their source regions? Contrib. Miner. Petrol. 106, 129–141.

Carmichael, I.S.E., Ghiorso, M.S., 1986. Oxidation–reduction relations in basic magma: a case for homogeneous equilibria. Earth Planet. Sci. Lett. 78, 200–210.

Carroll, M.R., Rutherford, M.J., 1987. The stability of igneous anhydrite: experimental results and implications for sulfur behavior in the 1982 eruption of El Chichon trachyandesite and other evolved magmas. J. Petrol. 28, 781–801.

Carroll, M.R., Rutherford, M.J., 1988. Sulfur speciation in hydrous experimental glasses of varying oxidation state: results from measured wavelength shifts of sulfur X-rays. Am. Mineral. 73, 845–849.

Carroll, M.R., Rutherford, M.J., 1985. Sulfide and sulfate saturation in hydrous silicate melts. J. Geophys. Res. 90, C601–C612.

Castillo, P.R., Janney, P.E., Solidum, R., 1999. Petrology and geochemistry of Camiguin Island, southern Philippines: Insight into the source of adakite and other lavas in a complex arc tectonic setting. Contrib. Miner. Petrol. 134, 33–51.

Chiaradia, M., 2014. Copper enrichment in arc magmas controlled by overriding plate thickness. Nat. Geosci. 7, 43–46.

Christie, D.M., Carmichael, I.S.E., 1986. Oxidation states of mid-ocean ridge basalt glasses. Earth Planet. Sci. Lett. 79, 397–411.

Clemente, B., Scaillet, B., Pichavant, M., 2004. The solubility of sulphur in hydrous rhyolitic melts. J. Petrol. 45, 2171–2196.

Cloos, M., 2001. Bubbling magma chambers, cupolas, and porphyry copper deposits. Int. Geol. Rev. 43, 285–311.

Cooke, D.R., Hollings, P., Walsh, J.L., 2005. Giant porphyry deposits: Characteristics, distribution, and tectonic controls. Econ. Geol. 100, 801–818.

Core, D.P., Kesler, S.E., Essene, E.J., 2006. Unusually Cu-rich magmas associated with giant porphyry copper deposits: evidence from Bingham, Utah. Geology 34, 41–44.

Corfu, F., Hanchar, J.M., Hoskin, P.W.O., Kinny, P., 2003. Atlas of zircon textures. Rev. Mineral. Geochem. 53, 469–500.

Crerar, D.A., Barnes, H.L., 1976. Ore solution chemistry V. solubilities of chalcopyrite and chalcocite assemblages in hydrothermal solution at 200° to 350°C. Econ. Geol. 71, 772–794.

Dalby, K.N., Anderson, A.J., Mariano, A.N., Gordon, R.A., Mayanovic, R.A., Wirth, R., 2010. An investigation of cathodoluminescence in albite from the A-type Georgeville granite, Nova Scotia. Lithos 114, 86–94.

Dawes, R.L., Evans, B.W., 1991. Mineralogy and geothermobarometry of magmatic epidote-bearing dikes, Front Range, Colorado. Geol. Soc. Am. Bull. 103, 1017–1031.

Defant, M.J., Drummond, M.S., 1993. Mount St. Helens: Potential example of the partial melting of the subducted lithosphere in a volcanic arc. Geology 21, 547–550.

Defant, M.J., Drummond, M.S., 1990. Derivation of some modern arc magmas by melting of young subducted lithosphere. Nature 347, 662–665.

DePaolo, D.J., 1981. Neodymium isotopes in the Colorado Front Range and crust-mantle evolution in the Proterozoic. Nature 291, 193–196.

Didier, J., Barbarin, B., 1991. Enclaves and Granite Petrology, Developments in Petrology. Elsevier Science Publications, Amsterdam pp 625.

Dong, L.H., Xu, X.W., Qu, X., Li, G.M., 2009. Tectonic setting and formation mechanism of the circum-Junggar porphyritic copper deposit belts. Acta Petrologica Sinica 25, 713–737.

Du, S.J., Qu, X., Deng, G., Zhang, Y., Cheng, S.L., Lu, H.F., Wu, Q., Xu, X.W., 2010.

Chronology and tectonic setting of intrusive bodies and associated porphyry copper deposit in the Hersai area, Eastern Junggar. Acta Petrologica Sinica 26, 2981–2996 (in Chinese with English abstract).
Evans, B.W., Vance, J.A., 1987. Epidote phenocrysts in dacitic dikes, Boulder County, Colorado. Contrib. Miner. Petrol. 96, 178–185.
Farrow, C.E.G., Barr, S.M., 1992. Petrology of high-Al-hornblende-and magmatic- epidote-bearing plutons in the southeastern Cape Breton High lands, Nova Scotia. Can. Mineral. 30, 377–392.
Fenn, P.M., 1986. On the origin of graphic granite. Am. Mineral. 71, 325–330.
Field, C.W., 1966. Sulfur isotope abundance data, Bingham district, Utah. Econ. Geol. 61, 850–971.
Finch, A., Klein, J., 1999. The causes and petrological significance of cathodoluminescence emission from alkali feldspars. Contrib. Miner. Petrol. 135, 234–243.
Frost, D.J., McCammon, C.A., 2008. The redox state of earth's mantle. Annu. Rev. Earth Planet. Sci. 36, 389–420.
Gao, S., Rudnick, R.L., Yuan, H.L., Liu, X.M., Liu, Y.S., Xu, W.L., Ling, W.L., Ayers, J., Wang, X.C., Wang, Q.H., 2004. Recycling lower continental crust in the North China craton. Nature 432, 892–897.
Goldstein, S.L., O'Nions, R.K., Keith, R., Hamilton, P.J., 1984. A Sm–Nd isotopic study of atmospheric dusts and particulates from major river systems. Earth Planet. Sci. Lett. 70, 221–236.
Goolaerts, A., Mattielli, N., de Jong, J., Weis, D., Scoates, J.S., 2004. Hf and Lu isotopic reference values for the zircon standard 91500 by MC–ICP–MS. Chem. Geol. 206, 1–9.
Götze, J., 2012. Application of cathodoluminescence microscopy and spectroscopy in Geosciences. Microsc. Microanal. 18, 1270–1284.
Halter, W.E., Pettke, T., Heinrich, C.A., 2002. The origin of Cu/Au ratios in porphyry-type ore deposits. Science 296, 1844–1846.
Harris, A.C., Kamenetsky, V.S., White, N.C., Achterbergh, E.V., Ryan, C.G., 2003. Melt inclusions in veins: Linking magmas and porphyry Cu deposits. Science 302, 2109–2111.
Harris, A.C., Kamenetsky, V.S., White, N.C., Steele, D.A., 2004. Volatile phase separation in silicic magmas at Bajo de la Alumbrera porphyry Cu-Au Deposit, NW Argentina. Resour. Geol. 54, 341–356.
Hattori, K.H., Keith, J.D., 2001. Contribution of mafic melt to porphyry copper mineralization: evidence from Mount Pinatubo, Philippines, and Bingham deposit, Utah. Miner. Deposita 36, 799–806.
Hedenquist, J.W., Lowenstern, J.B., 1994. The role of magmas in the formation of hydrothermal ore deposits. Nature 370, 519–527.
Heinrich, C.A., Driesner, T., Stefánsson, A., Seward, T.M., 2004. Magmatic vapor contraction and the transport of gold from the porphyry environment to epithermal ore deposits. Geology 32, 761–764.
Heinrich, C.A., Ryan, C.G., Mernagh, T.P., Eadington, P.J., 1992. Segregation of ore metals between magmatic brine and vapor – a fluid inclusion study using PIXE microanalysis. Econ. Geol. 87, 1566–1583.
Hemley, J.J., Cygan, G.L., Fein, J.B., Robinson, G.R., d'Angelo, W.M., 1992. Hydrothermal ore-forming processes in the light of studies in rock-buffered systems–I. Iron-copper-zinc-lead sulfide solubility relations. Econ. Geol. 87, 1–22.
Henley, R.W., King, P.L., Wykes, J.L., Renggli, C.J., Brink, F.J., Clark, D.A., Troitzsch, U., 2015. Porphyry copper deposit formation by sub-volcanic sulphur dioxide flux and chemisorption. Nat. Geosci. 8, 210–215.
Holzheid, A., Lodders, K., 2001. Solubility of copper in silicate melts as function of oxygen and sulfur fugacities, temperature, and silicate composition. Geochim. Cosmochim. Acta 65, 1933–1951.
Hong, T., Klemd, R., Gao, J., Xiang, P., Xu, X.W., You, J., Wang, X.S., Wu, C., Li, H., Ke, Q., 2017. The tectonic evolution of the Irtysh tectonic belt: new zircon U-Pb ages of arc-related and collisional granitoids in the Kalaxiangar tectonic belt, NW China. Lithos 272–273, 46–68.
Hong, T., Xiang, P., You, J., Zhang, L.C., Wu, Q., Zhang, G.L., Xu, X.W., 2015. The texture and formation age of the eastern Irtysh collision belt. Acta Petrologica Sinica 31, 571–593 (in Chinese with English abstract).
Jahn, B.M., Natal'in, B.A., Windley, B.F., Dobretsov, N., 2004. Phanerozoic continental growth in Central Asia. Jo. Asian Earth Sci. 23, 599–603.
Jahn, B.M., Wu, F., Chen, B., 2000. Granitoids of the central asian orogenic belt and continental growth in the phanerozoic. Trans. Royal Soc. Edinburgh: Earth Sci. 91, 181–193.
Jego, S., Pichavant, M., Mavrogenes, J.A., 2010. Controls on gold solubility in arc magmas: an experimental study at 1000 & #xB0;C and 4 kbar. Geochim. Cosmochim. Acta 74, 2165–2189.
Jenner, F.E., O'Neill, H., St, C., Arculus, R.J., Mavrogenes, J.A., 2010. The magnetite crisis in the evolution of arc-related magmas and the initial concentration of Au, Ag and Cu. J. Petrol. 51, 2445–2464.
Jian, P., Liu, D.Y., Zhang, Q., Zhang, F.Q., Shi, Y.R., Shi, G.H., Zhang, L.Q., Tao, H., 2003. SHRIMP dating of ophiolite and leucocratic rocks within ophiolite. Earth Sci. Front. 10, 439–456 (in Chinese with English abstract).
Jiang, N., Liu, Y.S., Zhou, W.G., Yang, J.H., Zhang, S.Q., 2007. Derivation of Mesozoic adakitic magmas from ancient lower crust in the North China craton. Geochim. Cosmochim. Acta 71, 2591–2608.
Johnson, E.R., Wallace, P.J., Cashman, K.V., Granados, H.D., 2010. Degassing of volatiles ($H_2O$, CO2, S, Cl) during ascent, crystallization, and eruption of basaltic magmas in the central Trans-Mexican Volcanic Belt. J. Volcanol. Geoth. Res. 197, 225–238.
Johnson, E.R., Wallace, P.J., Cashman, K.V., Granados, H.D., Kent, A.J.R., 2008. Magmatic volatile contents and degassing-induced crystallization at Volcan Jorullo, Mexico: implications for melt evolution and the plumbing systems of monogenetic volcanoes. Earth Planet. Sci. Lett. 269, 477–486.
Jugo, P.J., 2009. Sulfur content at sulfide saturation in oxidized magmas. Geology 37, 415–418.
Jugo, P.J., Luth, R.W., Richards, J.P., 2005. An experimental study of the sulfur content in basaltic melts saturated with immiscible sulfide or sulfate liquids at 1300°C and 1.0 GPa. J. Petrol. 46, 783–798.
Jugo, P.J., Wilke, M., Botcharnikov, R.E., 2010. Sulfur K-edge XANES analysis of natural and synthetic basaltic glasses: Implications for S speciation and S content as function of oxygen fugacity. Geochim. Cosmochim. Acta 74, 5926–5938.
Kay, R.W., 1978. Aleutian magnesian andesites: melts from subducted Pacific Ocean crust. J. Volcanol. Geoth. Res. 4, 117–132.
Kay, S.M., Ramos, V.A., Marquez, M., 1993. Evidence in Cerro Pampa volcanic rocks for slab-melting prior to ridge-Trench Collision in South America. J. Petrol. 101, 703–714.
Keller, P., 1988. Dendritic phosphate minerals and their paragenetic relation to the silicate minerals of pegmatites from Namibia and from the Black Hills, South Dakota, U.S.A. Neues Jahrbuch Mineralium Abhandlungen 159, 249–281.
Khain, E.V., Bibikova, E.V., Salnikova, E.E., Kröner, A., Gibsher, A.S., Didenko, A.N., Degtyarev, K.E., Fedotova, A.A., 2003. The Palaeo-Asian ocean in the Proterozoic and early Palaeozoic: new geochronologic data and palaeotectonic reconstructions. Precambr. Res. 122, 329–358.
Leake, B.E., Woolley, A.R., Arps, C.E.S., Birch, W.D., Gilbert, M.C., Grice, J.D., Hawthorne, F.C., Kato, A., Kisch, H.J., Krivovichev, V.G., Linthout, K., Laird, J., Mandarino, J.A., Maresch, W.V., Nickel, E.H., Rock, N.M.S., Schumacher, J.C., Smith, D.C., Stephenson, N.C.N., Ungaretti, L., Whittaker, E.J.W., Youzhi, G., 1997. Nomenclature of amphiboles: report of the subcommittee on amphiboles of the International Mineralogical Association, Commission on New Minerals and Mineral Names. Mineral. Mag. 61, 295–321.
Lee, C.T.A., Leeman, W.P., Canil, D., Li, Z.X.A., 2005. Similar V/Sc systematics in MORB and arc basalts: implications for the oxygen fugacities of their mantle source regions. J. Petrol. 46, 2313–2336.
Lee, C.T.A., Luffi, P., Chin, E.J., Bouchet, R., Dasgupta, R., Morton, D.M., Roux, V.L., Yin, Q.Z., Jin, D., 2012. Copper systematics in arc magmas and implications for crust-mantle differentiation. Science 336, 64–68.
Lee, C.T.A., Luffi, P., Roux, V.L., Dasgupta, R., Albaréde, F., Leeman, W.P., 2010. The redox state of arc mantle using Zn/Fe systematics. Nature 468, 681–685.
Lesher, C.E., 1990. Decoupling of chemical and isotopic exchange during magma mixing. Nature 344, 235–237.
Li, X.H., Tang, G.Q., Guo, B., Yang, Y.H., Hou, K.J., Hu, Z.C., L, Q.L., Liu, Y., Li, W.X., 2013. Qinghu zircon: a working reference for microbeam analysis of U-Pb age and Hf and O isotopes. Chinese Sci. Bull. 58, 1954–1961 (in Chinese).
Li, X.H., Liu, Y., Li, Q.L., Guo, C.H., Chamberlain, K.R., 2009. Precise determination of Phanerozoic zircon Pb/Pb age by multi-collector SIMS without external standardization. Geochem. Geophys. Geosyst. 10, Q04010. http://dx.doi.org/10.1029/2009GC002400.
Liou, J.G., 1973. Synthesis and stability relations of epidote, $Ca_2Al_2FeSi_3O_{12}(OH)$. J. Petrol. 14, 381–413.
Liu, Y.R., Jian, P., Zhang, W., Shi, Y.R., Wang, Y.Z., Zhang, L.Q., Liu, D.Y., 2016. Zircon SHRIMP U-Pb dating and O isotope of the Beitashan ophiolitic mélange in the East Junggar, Xinjiang, and its geological significance. Acta Petrologica Sinica 32, 537–554.
London, D., 1996. Granitic pegmatites. Trans. Royal Soc. Edinburg Earth Sci. 87, 305–319.
Lowell, J.D., Guilbert, J.M., 1970. Lateral and vertical alteration-mineralization zoning in porphyry ore deposits. Econ. Geol. 65, 373–408.
Lowenstern, J.B., Mahood, G.A., Rivers, M.L., Sutton, S.R., 1991. Evidence for extreme partitioning of copper into a magmatic vapor phase. Science 252, 1405–1408.
Ludwig, K.R., 2001. Users' Manual for Isoplot/Ex rev. 2.49. Berkeley Geochronology Centre Special Publication No. 1a.
Luhr, J.F., Carmichael, I.S.E., 1985. Jon1110 Volcano, Michoacan, Mexico (1759–1774): the earliest stages of fractionation in talc-alkaline magmas. Contrib. Miner. Petrol. 90, 142–161.
Macpherson, C.G., Dreher, S.T., Thirwall, M.F., 2006. Adakites without slab melting: high pressure processing of basaltic island arc magma, Mindanao, the Philippines. Earth Planetary Sci. Lett. 243, 581–593.
Martin, H., 1999. Adakitic magmas: modern analoge of Archean granitoids. Lithos 46, 411–429.
Martin, H., Smithies, R.H., Rapp, R., Moyen, J.F., Champion, D., 2005. An overview of adakite, tonalite–trondhjemite–granodiorite (TTG), and sanukitoid: relationships and some implications for crustal evolution. Lithos 79, 1–24.
Mavrogenes, J.A., O'Neill, H.S.C., 1999. The relative effects of pressure, temperature and oxygen fugacity on the solubility of sulfide in mafic magmas. Geochim. Cosmochim. Acta 63, 1173–1180.
Métrich, N., Clocchiatti, R., 1996. Sulfur abundance and its speciation in oxidized alkaline melts. Geochim. Cosmochim. Acta 60, 4151–4160.
Métrich, N., Bertagnini, A., Landi, P., Rosi, M., 2001. Crystallization driven by decompression and water loss at Stromboli volcano (Aeolian island) Italy. J. Petrol. 42, 1471–1490.
Nadeau, O., 2015. Ore metals beneath volcanoes. Nat. Geosci. 8, 168–169.
Nadeau, O., Williams-Jones, A.E., Stix, J., 2010. Sulphide magma as a source of metals in arc-related magmatic hydrothermal ore fluids. Nat. Geosci. 3, 501–505.
Nelson, B.K., Depaolo, D.J., 1985. Rapid production of continental crust 1.7 to 1.9 by ago: Nd isotopic evidence from the basement of the North American mid-continent. Geol. Soc. Am. Bull. 96, 746–754.
O'Neill, H.S.T.C., Mavrogenes, J.A., 2002. The sulfide capacity and the sulfur content at sulfide saturation of silicate melts at 1400°C. J. Petrol. 43, 1049–1087.
Ohmoto, H., Lasaga, A.C., 1982. Kinetics of reactions between aqueous sulfates and sulfides in hydrothermal systems. Geochim. Cosmochim. Acta 46, 1727–1745.

Owen, J.V., 1991. Significance of epidote in orbicular diorite from the Grenville Front zone, eastern Labrador. Mineral. Mag. 55, 173–181.
Parkinson, I.J., Arculus, R.J., 1999. The redox state of subduction zones: insights from arc peridotites. Chem. Geol. 160, 409–423.
Parkinson, I.J., Arculus, R.J., Eggins, S.M., 2003. Peridotite xenoliths from Grenada, Lesser Antilles Island Arc. Contrib. Miner. Petrol. 146, 241–262.
Pearce, J.A., Harris, N.B.W., Tindle, A.G., 1984. Trace element discrimination diagrams for the tectonic interpretation of granitic rocks. J. Petrol. 25, 956–983.
Peccerillo, A., Taylor, S.R., 1976. Geochemistry of Eocene calc-alkaline volcanic rocks from the Kastamonu area, Northern Turkey. Contrib. Miner. Petrol. 58, 63–81.
Qu, X., Xu, X.W., Liang, G.L., Qu, W.J., Du, S.J., Jiang, N., Wu, H.P., Zhang, Y., Xiao, H., Dong, L.H., 2009. Geological and geochemical characteristics of the Mengxi Cu-Mo deposit and its constraint to tectonic setting of the Qiongheba magmatic arc in east Junggar, Xinjiang. Acta Petrologica Sinica 25, 765–776 (in Chinese with English abstract).
Ragland, P.C., 1989. Basic Analytical Petrology. Oxford University Press P. 384.
Richards, J.P., 2011. Magmatic to hydrothermal metal fluxes in convergent and collided margins. Ore Geol. Rev. 40, 1–26.
Richards, J.P., Kerrich, R., 2007. Adakite-like rocks: their diverse origins and questionable role in metallogenesis. Econ. Geol. 102, 537–576.
Ripley, E.M., Brophy, J.G., 1995. Solubility of copper in a sulfur-free mafic melt. Geochim. Cosmochim. Acta 59, 5027–5030.
Ripley, E.M., Brophy, J.G., Li, C., 2002. Copper solubility in a basaltic melt and sulfide liquid/silicate melt partition coefficients of Cu and Fe. Geochim. Cosmochim. Acta 66, 2791–2800.
Roberts, M., Pin, C., Clemens, J.D., Paquette, J.L., 2000. Petrogenesis of mafic to felsic plutonic rock associations: the calc-alkaline queiärigut complex, french pyrenees. J. Petrol. 41, 809–844.
Schiano, P., Clocchiatti, R., Shimizu, N., Maury, R.C., Jochum, K.P., Hofmann, A.W., 1995. Hydrous silica-rich melts in the sub-arcmantle and their relationship with erupted arc lavas. Nature 377, 595–600.
Schmidt, M.W., 1992. Amphibole composition in tonalite as a function of pressure: an experimental calibration of the Al-in-hornblende barometer. Contrib. Miner. Petrol. 110, 304–310.
Seedorff, E., Dilles, J.H., Proffett, J.M., Einaudi, M.T., Zurcher, L., Stavast, W.J.A., Johnson, D.A., Barton, M.D., 2005. Porphyry deposits: characteristics and origin of hypogene features. Econ. Geol. 100, 251–298.
Shelley, D., 1967. Myrmekite and myrmekite-like intergrowths. Mineral. Mag. 36, 491–503.
Shen, P., Hattori, K., Pan, H., Jackson, S., Seitmuratova, E., 2015. Oxidation condition and metal fertility of granitic magmas: zircon trace-element data from porphyry cu deposits in the central asian orogenic belt. Econ. Geol. 110, 1861–1878.
Sial, A.N., Toselli, A.J., Saavedra, J., Parada, M.A., Ferreira, V.P., 1999. Emplacement, petrological and magnetic susceptibility characteristics of diverse magmatic epidote-bearing granitoid rocks in Brazil, Argentina and Chile. Lithos 46, 367–392.
Sillitoe, R.H., 2010. Porphyry copper systems. Econ. Geol. 105, 3–41.
Simon, A.C., Ripley, E.M., 2011. The role of magmatic sulfur in the formation of ore deposits. Rev. Mineral. Geochem. 73, 513–578.
Stacey, J.S., Kramers, J.D., 1975. Approximation of terrestrial lead isotope evolution by a two-stage model. Earth Planet. Sci. Lett. 26, 207–221.
Sun, W.D., Arculus, R.J., Kamenetsky, V.S., Binns, R.A., 2004. Release of gold-bearing fluids in convergent margin magmas prompted by magnetite crystallization. Nature 431, 975–978.
Tangeman, J.A., Lange, R., Forman, L., 2001. Ferric-ferrous equilibria in K2O-FeO-Fe2O3-SiO2 melts. Geochim. Cosmochim. Acta 65, 1809–1819.
Thornber, C.R., Roeder, P.L., Foster, J.R., 1980. The effect of composition on the ferric-ferrous ratio in basaltic liquids at atmospheric pressure. Geochim. Cosmochim. Acta 44, 525–532.
Titley, S.R., Beane, R.E., 1981. Porphyry copper deposits. Econ. Geol. 75, 214–269.
Tong, Y., Wang, T., Siebel, W., Hong, D.W., Sun, M., 2012. Recognition of early Carboniferous alkaline granite in the southern Altai orogen: post-orogenic processes constrained by U-Pb zircon ages, Nd isotopes, and geochemical data. Int. J. Earth Sci. 101, 937–950.
Tulloch, A.J., 1979. Secondary Ca-Al silicates as low grade alteration products of granitoid biotite. Contrib. Miner. Petrol. 69, 108–117.
Turkdogan, E.T., 1983. Physicochemical Properties of Molten Slags and Glasses. Metals Society, London, pp. P. 345.
Ulrich, T., 2002. Evolution of a porphyry Cu-Au deposit, based on LA-ICP-MS analysis of fluid inclusions, Bajo de la Alumbrera, Argentina. Econ. Geol. 97, 1888–1920.
Vernon, R.H., 2004. A Practical Guide to Rock Microstructure. Oxford University Press, Oxford0-521-89133-7 P46-101.
Vyhnal, C.R., McSween Jr., H.Y., Speer, J.A., 1991. Hornblende chemistry in southern Appalacian granitoids: implications for aluminum hornblende thermobarometry and magmatic epidote stability. Am. Mineral. 76, 176–188.
Wallace, P.J., Gerlach, T.M., 1994. Magmatic vapor source for sulfur dioxide released during volcanic eruptions: evidence from mount pinatubo. Science 265, 497–499.
Wallace, P.J., 2005. Volatiles in subduction zone magmas: concentrations and fluxes based on melt inclusion and volcanic gas data. J. Volcanol. Geoth. Res. 140, 217–240.
Wallace, P.J., Edmonds, M., 2011. The sulfur budget in magmas: evidence from melt inclusions, submarine glasses, and volcanic gas emissions. Rev. Mineral. Geochem. 73, 215–246.
Wang, Q., Xu, J.F., Jian, P., Bao, Z.W., Zhao, Z.H., Li, C.F., Xiong, X.L., Ma, J.L., 2006. Petrogenesis of adakitic porphyries in an extensional tectonic settings in Dexing, South China: implications for the genesis of porphyry copper mineralization. J. Petrol. 46, 119–144.
Wang, Q., McDermott, F., Xu, J.F., Bellon, H., Zhu, Y.T., 2005. Cenozoic K-rich adakitic volcanics in the Hohxil area, northern Tibet: lower crustal melting in an intracontinental setting. Geology 33, 465–468.
Wendlandt, R.F., 1982. Sulfide saturation of basalt and andesite melts high pressures and temperatures. Am. Mineral. 67, 877–885.
Wiedenbeck, M., Alle, P., Corfu, F., Griffin, W.L., Meier, M., Oberli, F., Vonquadt, A., Roddick, J.C., Speigel, W., 1995. Three natural zircon standards for U-Th–Pb, Lu–Hf, trace-element and REE analyses. Geostand. Newslett. 19, 1–23.
Wilkinson, J.J., 2013. Triggers for the formation of porphyry ore deposits in magmatic arcs. Nat. Geosci. 6 (11), 917–925.
Winter, J.D., 2001. An introduction to igneous and metamorphic petrology. Prentice Hall 150–210.
Woodhead, J., Hergt, J., Shelley, M., Eggins, S., Kemp, R., 2004. Zircon Hf-isotope analysis with an excimer laser, depth profiling, ablation of complex geometries, and concomitant age estimation. Chem. Geol. 209, 121–135.
Wu, F.Y., Yang, Y.H., Xie, L.W., Yang, J.H., Xu, P., 2006. Hf isotopic compositions of the standard zircons and baddeleyites used in U-Pb geochronology. Chem. Geol. 234, 105–126.
Xiao, W.J., Windley, B.F., Yuan, C., Sun, M., Han, C.M., Lin, S.F., Chen, H.L., Yan, Q.R., Liu, D.Y., Qin, K.Z., Li, J.L., Sun, S., 2009. Paleozoic multiple subduction-accretion processes of the southern Altaids. Am. J. Sci. 309, 221–270.
Xu, J.F., Shinjio, R., Defant, M.J., Wang, Q., Rapp, R.P., 2002. Origin of Mesozoic adakitic intrusive rocks in the Ningzhen area of east China: partial melting of delaminated lower continental crust? Geology 12, 1111–1114.
Xu, X.W., Dong, L.H., Qu, X., Liang, G.H., Liang, G.L., Zhang, L.C., Deng, G., Zhou, G., Xu, M.S., Xiao, Q.B., 2013a. Metallogenetic regularity and prognosis of porphyry copper deposits in the East Junggar. Geological Publishing House, Beijing. Pp275 (in Chinese).
Xu, X.W., Jiang, N., Li, X.H., Qu, X., Zhou, G., Dong, L.H., 2015a. Spatial-temporal framework for the closure of the Junggar Ocean in central Asia: New SIMS zircon U-Pb ages of the ophiolitic mélange and collisional igneous rocks in the Zhifang area, East Junggar. J. Asian Earth Sci. 111, 470–491.
Xu, X.W., Jiang, N., Li, X.H., Yang, Y.H., Mao, Q., Wu, Q., Zhang, Y., Dong, L.H., 2013b. Tectonic evolution of the East Junggar terrane: evidence from the Taheir tectonic window, Xinjiang, China. Gondwana Res. 24, 578–600.
Xu, X.W., Jiang, N., Yang, K., Zhang, B.L., Liang, G.H., Mao, Q., Li, J.X., Du, S.J., Ma, Y.G., Zhang, Y., Qin, K.Z., 2009. Accumulated phenocrysts and origin of feldspar porphyry in the Chanho area, western Yunnan, China. Lithos 113, 595–611.
Xu, X.W., Li, X.H., Jiang, N., Li, Q.L., Qu, X., Yang, Y.H., Zhou, G., Dong, L.H., 2015b. Basement nature and origin of the Junggar terrane: new zircon U-Pb-Hf isotope evidence from Paleozoic rocks and their enclaves. Gondwana Res. 28, 288–310.
Xu, X.W., Mao, Q., Li, X.H., Qu, X., Deng, G., Chen, D.Z., Zhang, B.L., Dong, L.H., 2014. Copper-zinc albite porphyry in the Hersai porphyry copper deposit, East Junggar, China: a transition between late magmatic and hydrothermal porphyry copper deposit. Ore Geol. Rev. 61, 141–156.
Xu, X.W., Peters, S.G., Liang, G.H., Zhang, B.L., 2016. Elastic stress transmission and transformation (ESTT) by confined liquid: a new mechanics for fracture in elastic lithosphere of the earth. Tectonophysics 672–673, 129–138.
Xu, X.W., Wu, Q., Huang, X.F., Liu, J., Zhang, Y., 2012. Formation mechanism and evolution process of copper-rich porphyry magma. Acta Petrologica Sinica 28, 421–432 (in Chinese with English abstract).
Yogodzinski, G.M., Kay, R.W., Volynets, O.N., Koloskov, A.V., Kay, S.M., 1995. Magnesian andesite in the western Aleutian Komandorsky region: implications for slab melting and processes in the mantle wedge. Geol. Soc. Am. Bull. 107, 505–519.
Yu, K.M., Boggs, S., Seyedolali, A., Ko, J., 1997. Albitization of feldspars in sandstones from the Gohan (Permian) and Donggo (Permo-Triassic) formations, Gohan area, Kangwondo, Korea. Geosci. J. 1, 26–31.
Zajacz, Z., Seo, Z.H., Candela, P.A., Piccoli, P.M., Heinrich, C.A., Guillong, M., 2010. Alkali metals control the release of gold from volatile-rich magmas. Earth Planet. Sci. Lett. 297, 50–56.
Zavaritsky, A.N., 1927. Classification of magmatic ore deposits. Econ. Geol. 22, 678–686.
Zeng, L., Niu, H., Bao, Z., Shan, Q., Li, H., Li, N., Yang, W., 2015. Petrogenesis and tectonic significance of the plagiogranites in the Zhaheba ophiolite, Eastern Junggar orogen, Xinjiang, China. J. Asian Earth Sci. 113, 137–150.
Zhang, Y., Liang, G.L., Wu, Q.Y., Wu, Q., Zhang, Z.F., Wu, H.P., Qu, X., Xu, X.W., 2010. Gechronology and Hf isotope evidences for early paleozoic magmatism in the Qiongheba area, East Junggar, Xinjiang, China. Acta Petrologica Sinica 25, 2389–2398 (in Chinese with English abstract).
Zhang, Y.Y., Guo, Z.J., 2010. New constraints on formation ages of ophiolites in northern Junggar and comparative study on their connection. Acta Petrologica Sinica 26, 421–430 (in Chinese with English abstract).
Zhang, Y., Pe-Piper, G., Piper, D.J.W., Guo, Z., 2013. Early Carboniferous collision of the Kalamaili orogenic belt, North Xinjiang, and its implications: Evidence from molasse deposits. GSA Bullet. 125, 932–944.
Zindler, A., Hart, S., 1986. Chemical geodynamics. Annu. Rev. Earth Planet. Sci. 14, 493–572.